REVIEW

Lithium Ion Batteries

Energy & Environmental Materials WILEY

Cobalt-Free Single-Crystal Cathodes for Next-Generation Lithium-Ion Batteries

Srinivasan Alagar, Rakesh Saroha, Jun Kim, Hyung Do Kim, Jung Sang Cho, and Sang Mun Jeong**

The transition toward sustainable, high-energy density lithium-ion batteries (LIBs) has intensified the search for cobalt-free cathode materials, driven by the environmental, economic, and ethical limitations associated with cobalt usage. Among these, single-crystal (SC) cobalt-free cathodes have emerged as a transformative class of materials, offering superior structural integrity, enhanced thermal stability, and prolonged cycling life. This review critically examines recent advancements in SC cathode architectures across four major material families: Ni-rich layered oxides, Li-Mn-rich compositions, spinel-type structures, and olivine-based frameworks. Unlike their polycrystalline analogues, SC cathodes feature continuous crystal lattices without internal grain boundaries, significantly reducing particle fracture, mitigating surface degradation, and suppressing phase instability during high-voltage cycling. We explore state-of-the-art synthesis techniques including molten salt-assisted crystallization, hydrothermal growth, and co-precipitation that enable the fabrication of phase-pure SC particles with tailored morphology and minimal defect content. Additionally, the role of structural tuning strategies such as elemental doping, surface coatings, and facet orientation control is discussed in detail, with particular emphasis on improving electrochemical reversibility, lithium-ion diffusion, and interfacial compatibility. Despite notable progress, key challenges persist, including controlling anisotropic lithium transport, preventing oxygen evolution, and ensuring process scalability. Emerging solutions involving entropy stabilization and advanced interface engineering are also discussed as promising pathways forward. By integrating insights across structure, chemistry, and processing, this review provides a comprehensive foundation for the design and deployment of cobalt-free SC cathodes, offering practical pathways toward safer, longer-lasting, and more sustainable LIB systems, compatible with both liquid and solid-state battery technologies.

1. Introduction

To mitigate the escalating depletion of fossil fuels and address the intensifying environmental challenges, there is a growing need to develop clean, high-performance energy storage technologies based on electrochemical principles.[1–3] Among these, lithium-ion batteries (LIBs) have become the cornerstone of modern energy storage due to their high energy density, long cycle life, minimal memory effect, and excellent operational reliability.[4–6] Over the past three decades, LIBs have found widespread application across diverse sectors, including mobile electronics, electric vehicles (EVs), and smart grid systems.[7,8]

The performance and longevity of LIBs are intimately governed by the cathode material, which remains a key determinant of the cell's energy density, voltage profile, and thermal stability. A variety of cathode chemistries have been employed in commercial and experimental LIBs, including $LiCoO_2$ (LCO), $LiFePO_4$, $LiMn_2O_4$, $LiNi_{0.5}Mn_{1.5}O_4$ (LNMO), nickel-rich layered oxides, and lithium-rich layered oxides (LLOs).[9,10] Among them, LCO set an early benchmark for volumetric energy density due to its high packing density (~4.2 g cm^{-3}) and stable voltage platform (~3.9 V).[11,12] However, the rising cost of cobalt and concerns regarding its supply chain sustainability, ethical mining practices, and geopolitical risks have accelerated the shift toward cobalt-free alternatives.

Dr. S. Alagar, J. Kim, Prof. S. M. Jeong
Department of Chemical Engineering, Chungbuk National University, Cheongju, Chungbuk 28644, Korea
E-mail: smjeong@chungbuk.ac.kr
Dr. R. Saroha, Prof. J. S. Cho
Department of Engineering Chemistry, Chungbuk National University, Cheongju-si, Chungbuk 28644, Korea
E-mail: jscho@cbnu.ac.kr
Dr. R. Saroha
Department of Materials Science and Engineering, Ajou University, Suwon 16499, Korea
Prof. H. D. Kim
Department of Polymer Chemistry Graduate School of Engineering, Kyoto University, Katsura Campus, Kyoto 615-8510, Japan
Prof. J. S. Cho
Biomedical Research Institute, Chungbuk National University Hospital, Cheongju, Chungbuk 28644, Korea
Prof. J. S. Cho, Prof. S. M. Jeong
Advanced Energy Research Institute, Chungbuk National University, Chungdae-ro 1, Seowon-gu, Cheongju 28644, Korea
The ORCID identification number(s) for the author(s) of this article can be found under https://doi.org/10.1002/eem2.70206.

DOI: 10.1002/eem2.70206

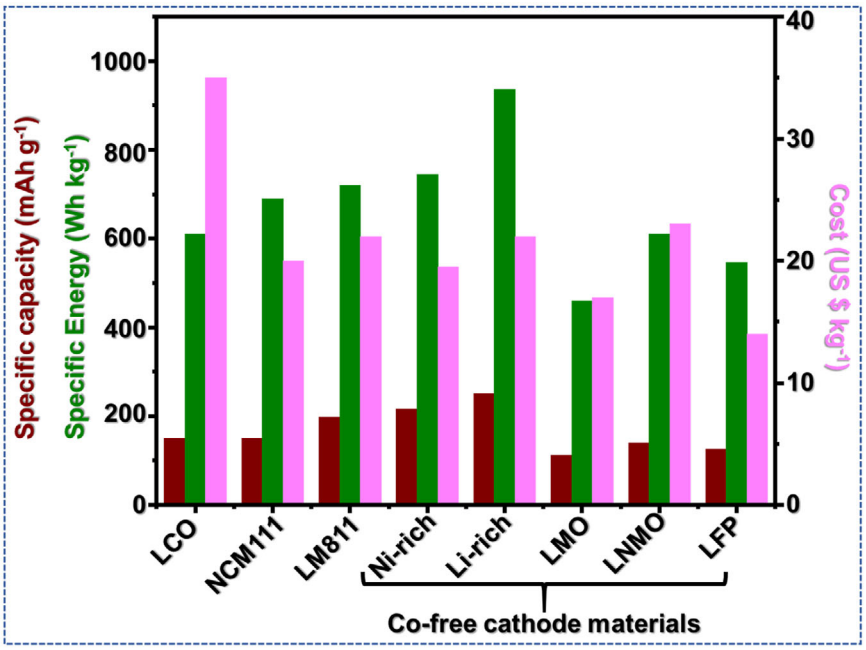

Figure 1. Comparison of major lithium-ion cathode materials LCO ($LiCoO_2$), NCM111 ($LiNi_{0.33}Co_{0.33}Mn_{0.33}O_2$), NCM811 ($LiNi_{0.8}Co_{0.1}Mn_{0.1}O_2$), LFP ($LiFePO_4$), LMO ($LiMn_2O_4$), LNMO ($LiNi_{0.5}Mn_{1.5}O_4$), Ni-rich ($Li[Ni_{0.9}Mn_{0.1}]O_2$), and Li-rich ($Li_{1.2}Ni_{0.2}Mn_{0.6}O_2$), highlighting differences in composition and cost. Considering the considerable fluctuations in material prices, the discussion here primarily refers to the study reported in published in 2020 year.[14]

Nickel-rich layered oxides (e.g., $LiNiO_2$-based compositions), Mn-rich and $LiFePO_4$-based compounds are now at the forefront of research into cobalt-free cathodes, offering a promising path toward cost-effective, high-capacity materials (**Figure 1**).[6,12–14] Nevertheless, these systems often suffer from structural instability, oxygen release, and surface degradation especially during high-voltage operation.[15] These issues are exacerbated in conventional polycrystalline forms, which consist of nanoscale primary particles aggregated into secondary structures.[16,17] Such architectures, although beneficial for lithium-ion transport, introduce grain boundaries that are prone to microcracking, electrolyte infiltration, and accelerated capacity fading.[18,19] To address these challenges, single-crystal cathodes (SCCs) have emerged as a structurally robust alternative. Unlike agglomerated secondary particles, SCCs are composed of discrete, micrometer or submicrometer-sized monocrystalline particles, featuring continuous lattice structures and minimized surface defects.[20–22] This morphology enhances mechanical strength, reduces the likelihood of intergranular cracking, and suppresses side reactions with liquid electrolytes.[19,23] While the term "single crystal" in this context is broader than the strict crystallographic definition, it typically refers to cathode particles with a uniform orientation, non-aggregated morphology, and clean grain boundary-free surfaces.[24] From a practical standpoint, cathode morphology significantly influences LIB manufacturability and performance. Spherical secondary agglomerates (SSAs) and single-crystal cathodes represent the two primary structural forms amenable to industrial-scale production. SSAs, composed of densely packed nanosized grains, generally offer high tap density and rate performance. However, they are vulnerable to long-term degradation due to interparticle fractures and gas release.[25,26] In contrast, SCCs exhibit superior structural integrity, better thermal stability, and more homogeneous electrochemical behavior, making them attractive for both conventional liquid electrolyte and next-generation solid-state battery systems.[27] In addition, a comparative evaluation of synthesis scalability has been incorporated, summarizing the practicality, environmental impact, and cost efficiency of molten-salt, co-precipitation, and hydrothermal routes, highlighting the industrial relevance of each for large-scale Co-free SCCs production.[28]

Despite their advantages, Co-free SCCs face certain limitations, including longer lithium-ion diffusion paths, local surface reactivity, and possible formation of microcracks at high rates or voltages. Therefore, extensive efforts have been directed toward optimizing synthesis techniques and developing modification strategies, such as lattice doping, crystal facet engineering, and surface coatings, to enhance their intrinsic stability and electrochemical performance. While numerous reviews have addressed cobalt-free cathodes, few have specifically examined the single-crystal approach. Emphasizing Co-free SCCs is particularly timely, as the drive toward cobalt-independent chemistries coincides with the industrial adoption of single-crystal particles to mitigate mechanical and interfacial degradation. This review bridges that gap by integrating cobalt elimination and single-crystal engineering into a unified, timely perspective. Here, we critically examine recent advances in Co-free SCCs, highlighting design principles, scalable synthesis strategies, and advanced surface and lattice modifications that enhance energy density, cycle life, and thermal stability. We further discuss their applicability in both liquid-electrolyte and solid-state configurations, while identifying persisting challenges and prospective directions for practical implementation.

2. Promising Candidates of Cobalt-Free Layered Cathodes

2.1. Cobalt Elimination Strategies for Single-Crystal Ni-Rich Layered Cathodes

Efforts to develop Co-free, Ni-rich layered cathodes have intensified following a comprehensive understanding of cobalt's pivotal role in early LIB materials. The pioneering work by Goodenough and co-workers on $LiCoO_2$ demonstrated its capability for efficient lithium extraction within the 3.0–4.3 V window vs. Li^+/Li,[11] establishing a benchmark for cathode performance. Cobalt's partially filled 3d orbitals supported an itinerant electron system that facilitated electronic delocalization, contributing to improved electrical conductivity and rate capability.[29] In systems like $LiNi_{1-x}Co_xO_2$, Ni serves as the primary redox-active species, with cobalt providing electrochemical buffering and enhanced structural coherence.[30] The development of ternary compositions such as $LiNi_{0.7}Co_{0.2}Mn_{0.1}O_2$ (NMC-721) introduced manganese for lattice stability, albeit electrochemically inactive,[31,32] while Co^{3+} further reduced Ni^{2+}/Li^+ cation intermixing and maintained conductivity.[33]

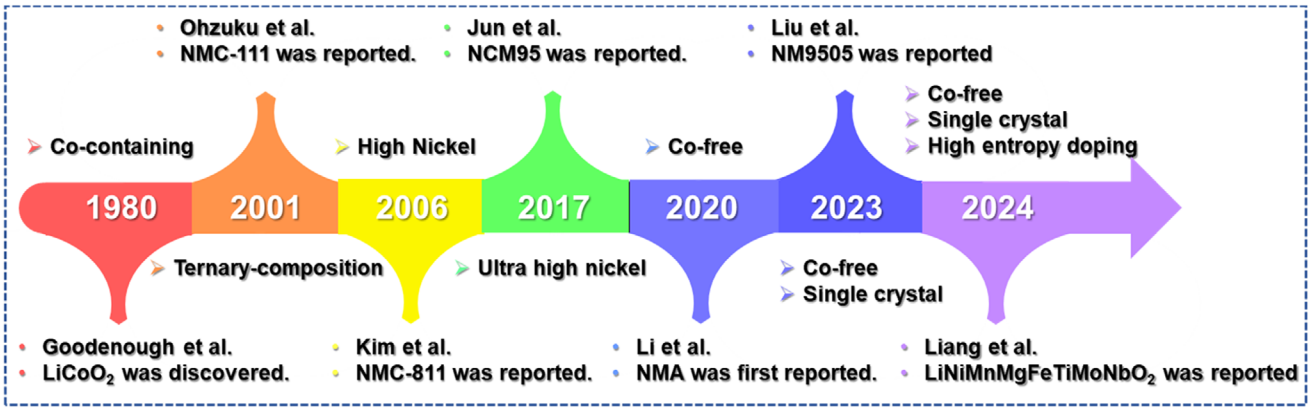

Figure 2. Timeline of cobalt elimination in Ni-rich layered cathodes from $LiCoO_2$ (1980),[11] to ternary NMC/NCA (2001),[33] high-Ni NMA (2006),[35] ultra-high nickel NCM95 (2017),[40] Co-free LiNiMn-based oxides (2020),[43] Co-free single-crystal $LiNiMnMgFeTiO_2$ (2023),[41] and the advent of Co-free single-crystal high-entropy cathodes (2024).[42]

Progressing toward higher energy density, materials like NMC-622 and NMC-811 increased Ni content, but challenges emerged including anisotropic volume changes, increased surface reactivity of Ni^{4+}, and moisture-induced degradation.[34–36] Alternatively, $LiNi_{1-xy}Co_xAl_yO_2$ (NCA) cathodes achieved high energy metrics, where Al substitution stabilized charge-transfer impedance and mitigated structural decay by lowering Ni's average oxidation state.[37–40] However, ethical concerns and geographical constraints surrounding cobalt extraction have driven the transition toward Co-free systems such as NM90 and NMA, which show competitive electrochemical performance but often struggle with long-term phase stability and particle fracture during cycling.[41,42] To overcome these limitations, recent progress has centered on single-crystal Co-free Ni-rich cathodes, which eliminate grain boundary-driven degradation and extend cycling stability.[43,44] The introduction of high-entropy element doping further enhances phase stability, suppresses structural collapse, and improves voltage tolerance.[41,42] This strategic shift from cobalt-rich polycrystalline materials to Co-free, Ni-rich single-crystal designs with entropy-driven stabilization is depicted in **Figure 2**, highlighting the next-generation direction for durable, high-capacity lithium-ion cathodes.

2.2. Crystal Structure and Single-Crystal Morphology of Co-Free Ni-Rich Cathode Materials

Co-free Ni-rich layered oxides, typically formulated as $LiNi_xM_{1-x}O_2$ (M = Mn, Al, Mg, etc.) have gained increasing attention as sustainable alternatives to conventional NCM materials.[9] These compounds crystallize in a rhombohedral R $\overline{3}$ m space group, adopting a structure analogous to α-$NaFeO_2$ (**Figure 3a**), where close-packed oxygen layers stack along the (111) cubic ((001) hexagonal) direction.[45] Lithium and transition metal (TM) ions occupy alternating octahedral sites, forming distinct TMO_2 slabs and interlayer Li planes. This O3-type layered framework exhibits an ABC oxygen stacking sequence, with site occupancies defined by $[Li]_{3b}[TM]_{3a}[O_2]_{6c}$ in Wyckoff notation.[12] In Ni-rich systems, the increasing ionic similarity between Li^+ (0.76 Å) and Ni^{2+} (0.69 Å) leads to significant cation disorder, which disrupts Li^+ diffusion pathways and destabilizes the layered framework.[46] The absence of Co, often used to mitigate such disorder and improve rate performance, further exacerbates the challenge of stabilizing the phase, especially under prolonged cycling.[47] In particular, low-spin Ni^{3+} ($t_{2g}^6e_g^1$) introduces Jahn–Teller distortion, promoting structural distortion and irreversible phase transitions.[48,49] Recent efforts have explored single-crystal morphologies as a promising route to address these issues, offering superior particle integrity, suppressed grain boundary cracking, and improved electrochemical resilience compared to conventional polycrystalline counterparts.

Electrochemical performance in these Co-free Ni-rich systems is primarily governed by the reversible redox transitions of $Ni^{2+}/Ni^{3+}/Ni^{4+}$, while Mn remains in a tetravalent state and serves a structural role. The crystal field splitting of TM d-orbitals in an octahedral ligand environment resulted in the separation into lower-energy t_{2g} and higher-energy e_g states (Figure 3b), with the latter being responsible for charge compensation during delithiation. Although high Ni content enables high theoretical capacities (>200 mA h g^{-1}), it also increases the risk of oxygen evolution, surface reconstruction, and thermal instability factors that significantly affect long-term performance. Layered oxide cathodes were typically engineered by adjusting the ratios of Ni, Co, and Mn to optimize electrochemical capacity, rate performance, and structural robustness (Figure 3c).[50] Partial substitution of Co and Mn with Ni^{2+} has been employed to mitigate Li^+/Ni^{2+} cation mixing and improve the stability of the bulk lattice. This approach has facilitated the development of NCM variants such as NCM333, NCM523, NCM622, and NCM811, which progressively increase Ni content to achieve higher specific capacities.[51] Despite these advancements, dependence on Co for enhancing rate capability and structural integrity continues to pose challenges in terms of cost and large-scale implementation. To overcome these limitations, electrochemically inactive dopants, including Al^{3+}, Mg^{2+}, and B^{3+}, have been introduced.[42,52] These elements occupy transition-metal sites, alleviate lattice strain, suppress cation disorder, and reduce phase transformations during repeated cycling, thereby reinforcing the layered framework. Recently, Liu et al. investigated the synthesis kinetics of single-crystal Co-free Ni-rich $LiNi_{0.95}Mn_{0.05}O_2$ (NM9505) particles, with their faceted morphology and grain-boundary-free nature, exhibit reduced surface area for parasitic reactions, and show improved phase stability under high-voltage operation.[41] The authors reported that the morphology of Ni-rich cathodes strongly depended on the synthesis route. As shown in Figure 3d,e, Scanning Electron Microscopy (SEM) images revealed polycrystalline particles with irregular shapes and significant

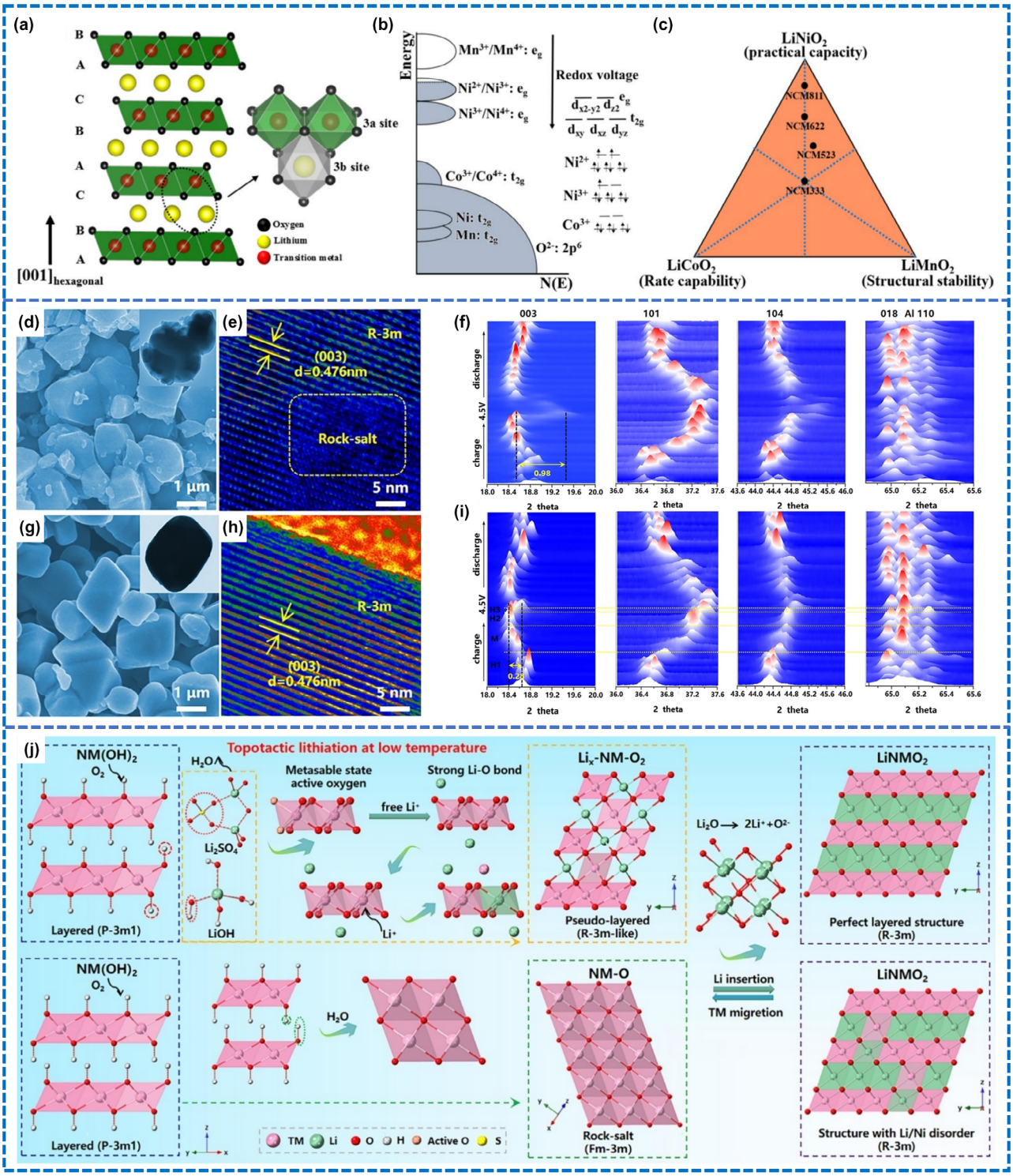

Figure 3. a) Crystal structure of layered $LiMO_2$. b) Electronic configurations in NCM oxides. c) Phase diagram showing TM ratio effects on electrochemical performance. a–c) were reproduced with permission.[17] Copyright 2021, Springer Nature. d, e) SEM and HRTEM of polycrystalline $LiNi_{0.95}Mn_{0.05}O_2$ (NM) showing irregular grains and rock-salt surface. f) In situ XRD of polycrystalline NM revealing large c-lattice shrinkage. g, h) Molten-salt-synthesized single-crystal NM showing faceted morphology and intact $R\bar{3}m$ lattice. i) In situ XRD of single-crystal NM with reduced lattice contraction. j) Topotactic lithiation mechanism via molten-salt route yielding ordered layered structures with suppressed Li/Ni disorder and oxygen loss. d–j) were reproduced with permission.[41] Copyright 2023 Wiley-VCH.

agglomeration, while High-Resolution Transmission Electron Microscopy (HR-TEM) images showed lattice distortions along the (003) plane and surface rock-salt phase formation, indicating the presence of structural defects. In contrast, for the molten salt approach (Figure 3g, h), both SEM and HR-TEM images showed the growth of uniform, faceted single crystals with well-defined particle shapes and continuous R $\overline{3}$ m layered domains, exhibiting minimal surface degradation and reduced defects. In situ X-ray Diffraction (XRD) studies (Figure 3f,i) reveal that molten-salt-synthesized single crystal NM9505 cathodes exhibit lower c-lattice contraction (≈1.0%) and reduced angular displacement during H2-H3 transitions, compared to their polycrystalline counterparts, which undergo a more severe contraction (≈2.1%) an indicator of enhanced structural reversibility under high-voltage cycling. The schematic in Figure 3j, illustrates the topotactic lithiation route during molten salt synthesis at low temperature, wherein metastable layered precursors (e.g., NMOH) evolve through an intermediate pseudo-layered Li-rich phase toward a stable layered R $\overline{3}$ m structure (LiNM-O_2), effectively suppressing unwanted rock-salt phase formation. This pathway not only promotes Li/TM ordering but also stabilizes the oxygen sublattice by preserving Li-O coordination and inhibiting O_2 release. Collectively, these observations highlighted that the combination of dopant chemistry, single-crystal morphology, and low-temperature topotactic lithiation via molten salt synthesis, along with controlled precursor co-precipitation, provided an effective strategy to mitigate cation disorder and surface reconstruction. Therefore, optimizing such synthesis approaches is critical for the preparation of durable single-crystal Co-free Ni-rich cathode materials, as discussed below.

2.3. Synthesis Methods for Co-Free Ni Rich Cathode Materials

The realization of Co-free, Ni-rich single-crystal layered oxides is closely dependent on the development of synthesis methods capable of delivering phase-pure structures with high crystallographic integrity and scalability for industrial translation. Multiple synthesis approaches have been employed, including co-precipitation,[9] solid-state reactions,[48] spray-drying,[53,54] solvothermal,[55,56] and sol–gel[57] methods, each imparting distinct control over particle size distribution, elemental homogeneity, and microstructural features. Solid-state synthesis remains cost-effective and straightforward but is often limited by poor mixing at the atomic scale, leading to compositional inhomogeneity. Spray-drying offers high-throughput production and spherical particle formation; however, rigorous post-calcination is necessary to achieve uniform phase development. Solvothermal and sol-gel approaches provide superior regulation of particle nucleation and growth, yielding well-dispersed and compositionally uniform powders, though their restricted scalability hampers practical application.

Among these methods, co-precipitation has emerged as the most versatile and technologically relevant strategy. Its ability to precisely tune transition-metal stoichiometry, regulate nucleation kinetics, and produce faceted, high-density precursors is particularly beneficial for stabilizing high-Ni, Mn-rich layered frameworks in the absence of cobalt.[58–60] Furthermore, this route suppresses cation disorder, mitigates surface reconstruction, and minimizes the formation of undesirable rock-salt domains. The inherent adaptability of co-precipitation to continuous-flow or large-scale reactor systems further strengthens its industrial viability.[61] Consequently, co-precipitation is widely regarded as the most promising pathway for constructing next-generation Co-free Ni-rich (CFNR) single-crystal cathode materials with improved thermal stability, extended cycle life, and compatibility with practical cell assembly.

2.4. Co-Free Ni-Rich Single Crystal Cathodes

Single-crystal engineering has emerged as a compelling strategy to enhance the structural integrity and electrochemical stability of CFNR layered oxide cathodes, circumventing the intrinsic microstructural limitations of their polycrystalline analogues.[62] In polycrystalline materials, repetitive lithiation and delithiation cycles often induce intergranular stress accumulation, leading to microcracking, particle fragmentation, and electrolyte infiltration into newly exposed surfaces, a phenomenon that accelerates surface reconstruction, TM dissolution, cathode–electrolyte interfacial (CEI) thickening, and phase transformation.[63] In contrast, single-crystal architectures eliminate internal grain boundaries, thereby suppressing the initiation and propagation of microcracks and promoting a more uniform stress distribution throughout the particle.[64] This cohesive lattice framework fundamentally mitigates structural degradation during long-term operation.[23]

In single-crystal cathodes, the absence of internal grain boundaries allows mechanical stress to be distributed more evenly throughout the lattice. This uniform stress accommodation suppresses microcrack initiation, prevents intergranular fracture, and helps maintain structural integrity over prolonged cycling.[64] However, the durability of these materials is not determined solely by their bulk stability. The electrochemical response is strongly influenced by the crystallographic facets exposed at the surface, since planes such as (003), (101), and (104) differ in surface energy, Li-ion transport pathways, and chemical reactivity toward electrolyte species. Facet-selective tailoring through molten-salt growth, dopant-driven segregation, or flux-assisted crystal shaping enables preferential exposure of Li-terminated, low-energy planes, which are intrinsically more resistant to electrolyte corrosion and high-voltage degradation.[23] These strategies demonstrate how control of surface orientation, in concert with bulk crystallinity, can substantially enhance the long-term stability of CFNR oxides.

Ni et al. reported that single-crystal design strategies significantly advanced the field of CFNR cathodes, offering superior resistance to microcracking and reversible phase transitions, particularly in high-Ni systems.[65] In CFNR $LiNi_{0.95}Mn_{0.05}O_2$ (SC-NM95), synthesized via co-precipitation followed by the molten-salt-mediated crystal growth method, the elimination of grain boundaries translates to enhanced mechanical robustness and mitigated H2-H3 induced stress (**Figure 4**a).[19,65,66] In contrast, conventional polycrystalline NM95 (PC-NM95) developed severe intergranular cracks during deep cycling, which triggered parasitic side reactions and facilitated the formation of NiO-like rock-salt domains, ultimately causing rapid capacity decay to 17.6% after 400 cycles. SC-NM95, owing to its monolithic architecture, uniformly accommodated volume changes, restrained phase-induced anisotropy, and preserved structural integrity, thereby retaining 54.5% of its capacity after 400 cycles at 5 C (2.7–4.3 V), as shown in Figure 4b.[67] These findings indicate that CFNR single crystals remain crack-free under high-voltage abuse and show superior capacity retention over polycrystalline.[19,68] The molten salt approach, widely reviewed in the context of Ni-rich cathode synthesis, enables controlled grain growth, improved facet development, and reduced Li/TM mixing by facilitating atom diffusion above 800 °C with appropriate Li-rich fluxes.[65,67,69] Liu et al. provide insights into the improved cycling

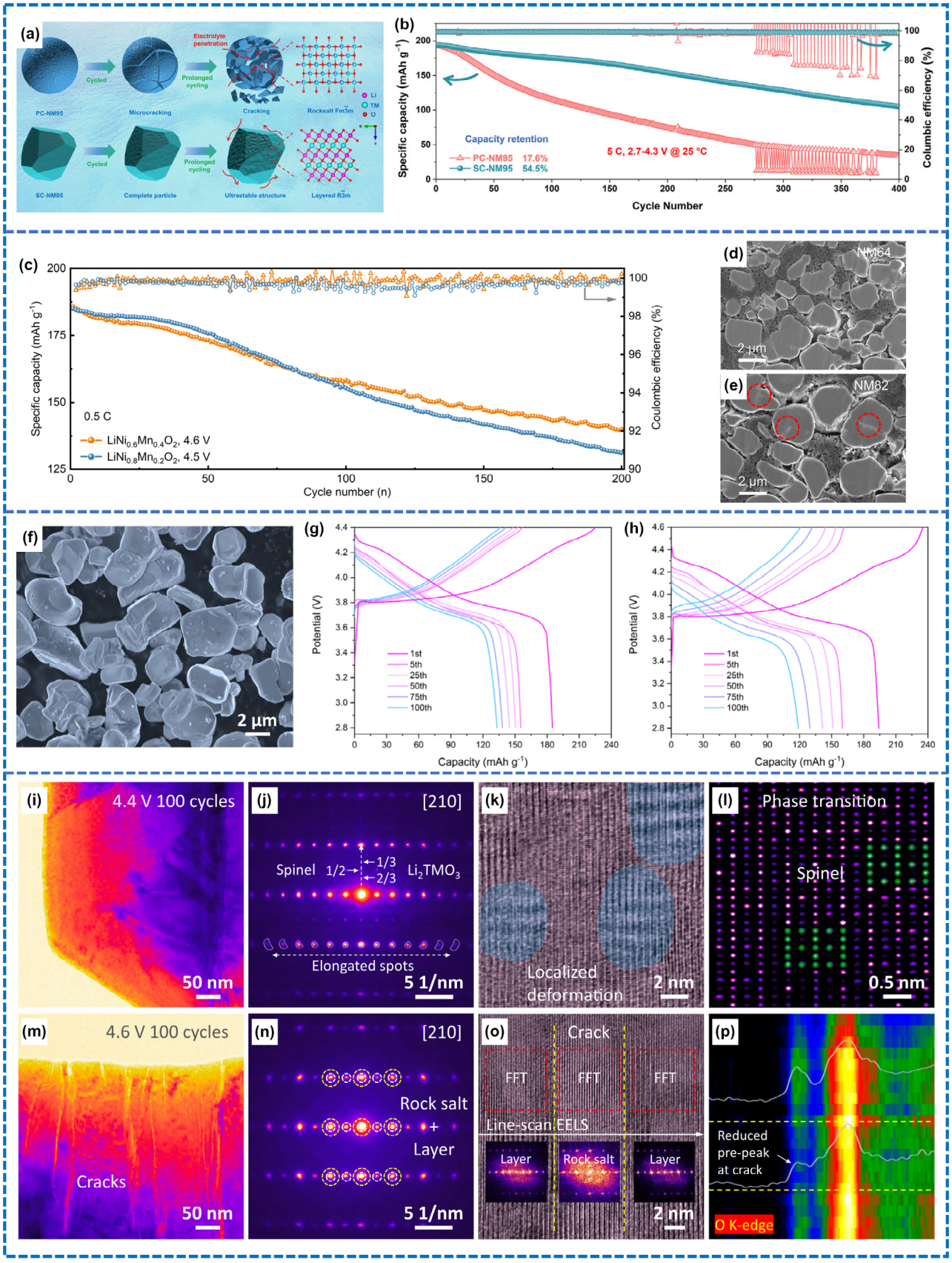

Figure 4. a) Schematic illustration of morphological evolution and degradation in PC-NM95 and SC-NM95 during prolonged cycling. b) Cycling performance of SC-NM95 at 5 C. a, b) were reproduced with permission.[65] Copyright 2022 Elsevier. c) Comparative cycling stability of NM64 and NM82 at 0.5 C. d, e) Cross-sectional SEM images of NM64 and NM82 after cycling, showing structural integrity differences. a–e) were reproduced with permission.[70] Copyright 2024 Royal Society of Chemistry. f) SEM image of synthesized SC75 particles. g, h) Charge/discharge profiles of SC75 at 2.8–4.4 V and 2.8–4.6 V, respectively. Post-cycling microscopic analysis of SC75, i) Low-magnification TEM of SC75 after 100 cycles at 0.5 C. j) SAED pattern indicating weak Li_2TMO_3 and emerging spinel reflections. k, l) HRTEM images from bulk regions revealing localized spinel transitions. m) TEM of SC75 after cycling at 2.8–4.6 V, showing severe particle cracking. n) SAED indicating rock-salt phase formation. o) HR-TEM of the crack zone with structural transformation. p) EELS O K-edge line scan across the degraded region, confirming oxygen loss and phase transition. f–p) were reproduced with permission.[73] Copyright 2025 Springer Nature.

stability of CFNR cathodes, $LiNi_{0.64}Mn_{0.36}O_2$ (NM64) and $LiNi_{0.82}Mn_{0.18}O_2$ (NM82), highlighting the importance of Ni/Mn ratio tuning for achieving structural robustness and electrochemical stability under high-voltage operation.[70] NM64, despite its elevated cut-off voltage, exhibits superior capacity retention (85.1% vs. 83.7% after 100 cycles) and maintains 75.2% of its initial capacity after 200 cycles, surpassing NM82 (71.0%), as shown in Figure 4c. Microstructural (SEM) analysis (Figure 4d,e) reveals that NM64 preserves its dense morphology without evident microcrack formation, whereas NM82 suffers from prominent intragranular fractures, attributed to excessive anisotropic lattice stress.[71] Notably, the presence of moderate Li/Ni antisite disorder in NM64 plays a structural stabilization role by partially arresting slab collapse during cycling. Conversely, the high-valence Ni species in NM82 (Ni^{3+}/Ni^{4+}) promote oxygen evolution and facilitate an irreversible transition toward a rock-salt-type phase, accelerating capacity fading.[72] These observations collectively indicate that a Mn-rich composition with controlled Li/Ni disorder can serve as a promising strategy to suppress mechanical degradation and prolong high-voltage cycling life, while minimizing the reliance on expensive cobalt.

Yu et al. revealed that $LiNi_{0.75}Mn_{0.25}O_2$ (SC75), a CFNR layered oxide synthesized via co-precipitation followed by solid-state calcination, provides a good balance between structural stability and energy density.[73] SEM (Figure 4f) analysis reveals uniformly distributed particles in the 3–5 μm range, which may reduce intergranular fracture but also limit Li^+ diffusion and introduce initial structural defects. As shown in Figure 4g, the SC75 cathode delivers an initial discharge capacity of ~185 mA h g^{-1} at 0.1 C within 2.8–4.4 V, though with a relatively low initial Coulombic efficiency of 84%, which is inferior to that of typical co-containing single-crystal NMC counterparts. Upon cycling at 0.5 C, a slight capacity fade is observed. When the upper cut-off voltage is increased to 4.6 V (Figure 4h), a marginally higher initial capacity of ~194 mA h g^{-1} is achieved; however, this comes at the expense of worsened Coulombic efficiency and more pronounced electrochemical degradation, indicating structural instability under high-voltage operation. TEM analysis tracks structural changes in SC75 cathodes during cycling. After 100 cycles at 4.4 V, low-magnification TEM (Figure 4i) shows preserved particle morphology, while SAED (Figure 4j) confirms the layered structure with diminished Li_2TMO_3 phase and elongated diffraction spots indicating lattice strain. HR-TEM (Figure 4k,l) reveals moiré patterns and spinel phase formation driven by localized strain, oxygen loss, and TM migration, consistent with SXDM data. These Li-rich nanodomains (LRNDs) cause bulk lattice degradation distinct from surface reconstruction. At 4.6 V, pronounced intragranular cracks appear (Figure 4m). SAED (Figure 4n) shows complete Li_2TMO_3 loss and enhanced rock-salt phase. HR-TEM near cracks (Figure 4o) confirms rock-salt formation with TMs occupying lithium sites, causing capacity fade. Strain-induced cracking exposes fresh surfaces, accelerating irreversible phase transitions. EELS line scans (Figure 4p) confirm oxygen loss through reduced O K-edge prepack, supporting the role of LRNDs as buried defects that activate under high voltage, leading to lattice collapse and electrochemical decay.

The synthesis of such single-crystal CFNR particles typically involves high-temperature calcination assisted by low-melting lithium-based salts ($LiOH–Li_2SO_4$), which create a molten flux that facilitates dissolution–recrystallization processes (**Figure 5a**) and promotes the growth of phase-pure, faceted single grains.[63] A notable example includes the molten salt synthesis of $LiNi_{0.9}Mn_{0.1}O_2$ (SC-NM91), wherein Dai et al. achieved uniform, crack-free crystals (Figure 5b,c) exhibiting enhanced mechanical robustness and significantly improved electrochemical performance, demonstrated by a capacity retention of 87.72% after 300 cycles at 1 C within 3.0–4.3 V, outperforming the polycrystalline counterpart (65.53%) (Figure 5d). This improvement underscores the effectiveness of crystallographic continuity in resisting degradation pathways common in Ni-rich systems. Importantly, the realization of single-crystal cathode particles without relying on elemental doping marks a significant advancement, as it avoids potential complications associated with dopant-induced lattice distortion or electrochemical side effects.[21,41,74–78] Shen et al. developed a thermodynamically stabilized, single-crystal, cobalt-free Ni-rich layered oxide cathode tailored for high-voltage LIB.[21] By precisely tuning the composition and processing conditions, they demonstrated that the structural degradation typically associated with CFNR under elevated voltages (≥4.4 V) can be effectively suppressed. Their single-crystal design strategy mitigates intergranular cracking and phase transition instabilities, while achieving long-term cycling performance at high voltage windows. Figure 5e presented a schematic overview of the synthesis strategy of CFNR layered cathodes $LiNi_{0.8}Mn_{0.18}Fe_{0.02}O_2$ (NMF), which was developed via a co-precipitation method followed by one-step calcination and fluid-energy milling, yielding dense, monolithic particles with high crystallographic integrity. Electrochemical evaluation revealed that although NMF exhibits relatively lower capacity at 4.3 V compared to polycrystalline $LiNi_{0.83}Co_{0.11}Mn_{0.06}O_2$ (MNCM) and single-crystalline $LiNi_{0.83}Co_{0.11}Mn_{0.06}O_2$ (SNCM) (Figure 5f), its energy density significantly improved under elevated conditions (4.6 V, 55 °C), achieving 824.4 Wh kg^{-1}. Differential capacity plots show broadened and positively shifted H2-H3 redox peaks in NMF, indicating delayed phase transitions and alleviated anisotropic strain. The NMF electrode retained 84.5% of its capacity after 100 cycles at 4.6 V and 55 °C, far outperforming MNCM (which fails prematurely) and SNCM (54.8% retention). In pouch-type full cells, NMF delivers excellent cycling durability with 90.2% capacity retention after 600 cycles and stable voltage profiles at 4.35 V (Figure 5g), underscoring its thermal resilience. The authors demonstrated that morphological investigations uncovered marked intergranular cracking and disintegration in polycrystalline MNCM, whereas NMF maintains particle integrity and a stable R $\bar{3}$ m layered structure with only slight disorder offering a robust strategy for developing high-energy, thermally stable, CFNR cathodes for next-generation LIBs.

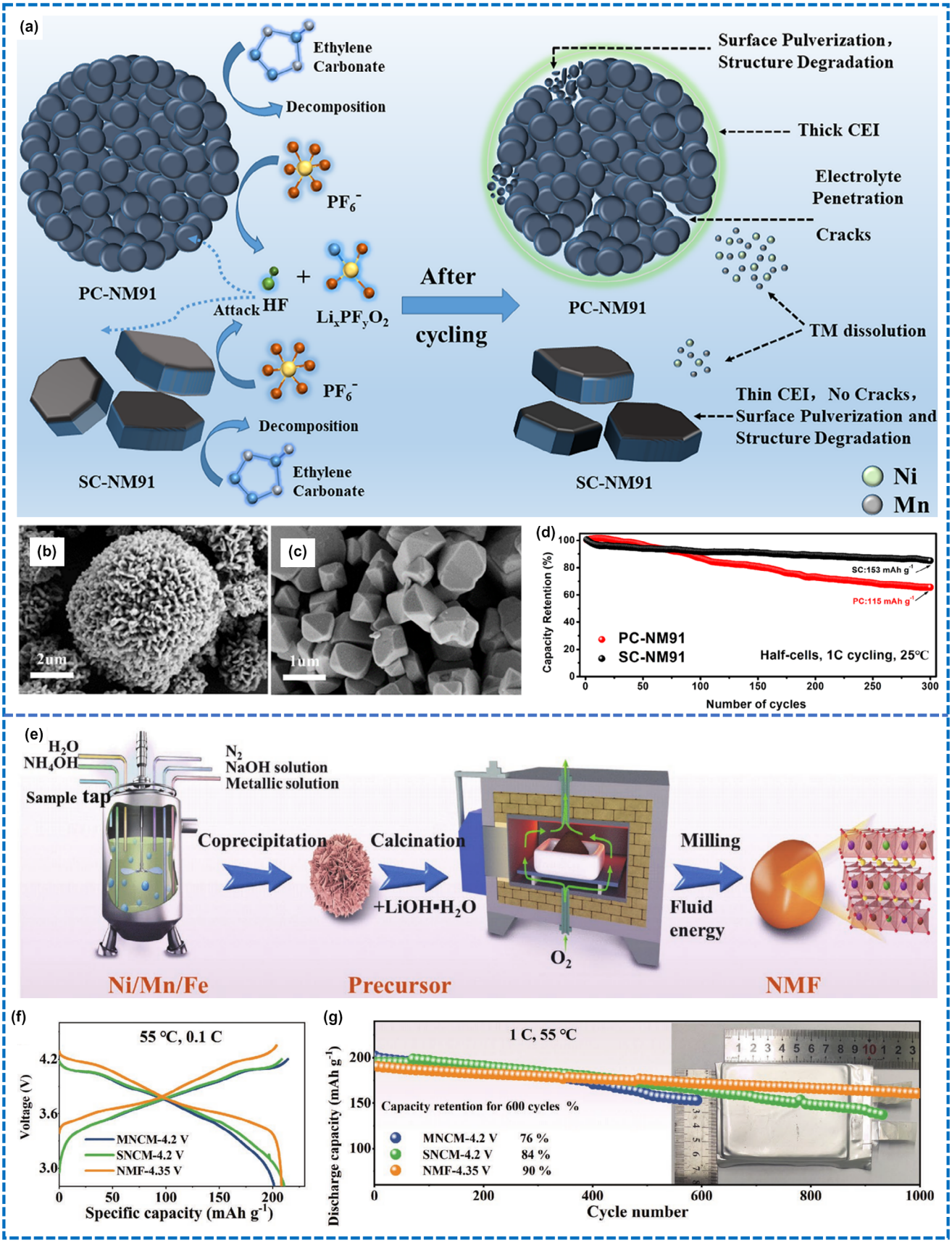

Figure 5. a) Schematic of single-crystal NM91 suppressing structural degradation and capacity fade. b, c) SEM images of PC-NM91 and SC-NM91 particles. d) Cycling stability at 1 C over 300 cycles, highlighting the durability of SC-NM91. a–d) were reproduced with permission.[74] Copyright 2022 American Chemical Society. e) Schematic representation of the synthetic process for single-crystal NMF materials. f) Initial charge–discharge profiles of the pouch-type full cell at 0.1 C. g) Long-term cycling performance at 1 C. e–g) were reproduced with permission.[21] Copyright 2023 Wiley-VCH.

2.5. Doping in Ni-Rich Cathode Materials

CFNR layered oxides face major challenges, including surface degradation, particle cracking, and rapid capacity fading, especially under high-voltage operation. To address these issues, researchers have developed various modification strategies focused on controlling both the bulk crystal structure and the surface chemistry of the particles. These modifications are particularly effective when applied to single-crystal cathodes, which naturally suppress grain boundary-driven degradation and microcrack propagation. Below, we review key advancements in elemental doping, surface coatings, and facet control that have transformed the electrochemical performance of these materials.

Saleem et al.[79] studied the elimination of cobalt and manganese, combined with precise Fe-Cu co-doping, which markedly strengthened the structural resilience of ultra–high-Ni single-crystal layered oxides. Morphological observations (**Figure 6**a,b) reveal that Co-Mn-free $LiNi_{0.94}Fe_{0.05}Cu_{0.05}O_2$ (SCNFCu) develops faceted, polyhedral single-crystal particles with smooth, defect-free surfaces. This grain-boundary-free configuration, together with controlled facet orientation, mitigated mechanical fatigue and suppressed surface reconstruction during extended high-voltage cycling. A narrow particle size distribution (1–3 μm), achieved via optimized high-temperature synthesis, enhanced uniformity, and prevented microcrack formation, thereby restricting electrolyte penetration and preserving lattice stability. Electrochemical testing revealed that $LiNi_{0.9}Mn_{0.05}Co_{0.05}O_2$ (SCNMC) and SCNFCu electrodes exhibit initial discharge capacities of approximately 211 and 220 mAh g^{-1}, respectively, at a 0.1 C rate (Figure 6c). Although the difference in capacity is slight, SCNFCu consistently shows improved performance. Long-term cycling at 1 C (Figure 6d) indicates capacity retentions of 89% for SCNMC and 93% for SCNFCu, highlighting the beneficial role of Fe-Cu co-doping on electrochemical stability. The long-term performance of the cathodes was evaluated in graphite-based pouch full cells. After 600 cycles at 1 C within 3.0–4.3 V, SCNFCu retained 77% of its initial capacity, significantly exceeding SCNMC, which retained only 66% (Figure 6e). These results highlight the superior cyclability and structural stability of SCNFCu in full-cell configurations. Structural analysis indicated that Fe preferentially occupied Co-like octahedral sites in the transition-metal slab, mitigating Li/Ni cation disorder and strengthening TM-O bonds, while Cu substituted Mn-rich sites, where its stronger Cu-O covalency further reinforced the oxygen framework (Figure 6f). When co-doped, Fe and Cu acted synergistically without site competition, thereby stabilizing the Ni-O network, reducing Li^+ diffusion length, and enhancing structural robustness.[80–82] The electronic structure trends (Figure 6g) were consistent with these lattice-level modifications. Fe and Cu incorporation shifted the Fermi level upward, increasing Ni-3d orbital occupancy, while Cu substitution enhanced Cu-O hybridization relative to Mn-O, indicating improved lattice oxygen stability. Additional Fe-O and Li-O interactions imparted rigidity, and these DOS modifications correlated with enhanced capacity retention, thermal stability, and long-term cycling in CFNR cathodes.[83–85]

Recent advances in facet engineering were reported to overcome the long-standing trade-offs between ionic transport, interface stability, and capacity retention in CFNR cathodes. A notable example was the tailored single-crystal, cobalt-free $LiNi_{0.718}Mn_{0.271}Al_{0.01}W_{0.001}O_2$ (NMAW), synthesized via wet-doping to regulate dopant distribution (Figure 6h). Al was uniformly incorporated into the lattice, while W migrated toward the particle surface, forming a core–shell structure with a (003) facet-rich core and a (104) facet shell. The (104) facet provided lower energy barriers for Li^+ transport, reduced polarization, and suppressed Li accumulation, while maintaining structural continuity during cycling. HR-TEM confirmed a 1–2 nm surface layer indexed to the (104) facet, in contrast to the (003) termination in undoped counterparts (Figure 6i). Electrochemical testing at 45 °C showed that NMAW retained 92% of its capacity after 100 cycles at 1 C, compared with 79% for NMA and 65% for NM (Figure 6j), with minimal polarization growth of NMAW (Figure 6k). Zhang et al. further demonstrated that trace W incorporation into CFNR cathodes enhanced both Li-ion transport and structural integrity.[86] The $Ni_{0.9}Mn_{0.1}(OH)_2$ precursor undergoes lithiation and two-step calcination to yield single-crystal SNM91-W3 particles. The introduction of ∼0.3 mol% WO_3 facilitated homogeneous W doping, producing an optimized phase with an initial discharge capacity of 209 mA h g^{-1} at 0.1 C, higher than undoped SNM91 (197 mAh g^{-1}).[86] Under cycling, SNM91-W3 retained 93.3% of capacity after 100 cycles at 0.2 C, compared with 78% for SNM91 and still maintained 84.4% retention after 200 cycles, significantly outperforming the SNM913 (Figure 6l). Full-cell configurations employing SNM91-W3 with graphite anodes delivered a discharge capacity of ∼208 mA h g^{-1} (0.1 C), and when cycled at 0.5 C for 200 cycles (Figure 6m), they retained 80.8% of the initial capacity, which was markedly higher than the 72.3% retention exhibited by the undoped SNM91. This substitution modulates the local electronic environment and reduces the migration barrier for Li-ion, thereby boosting ionic conductivity. Simultaneously, the high electronegativity and strong oxygen affinity of tungsten help stabilize the oxygen sublattice, suppressing lattice oxygen release during delithiation. This dual effect —kinetic enhancement and structural reinforcement—mitigates microcrack formation, suppresses transition-metal dissolution, and reduces surface reconstruction.

2.5.1. *Advanced High Entropy Doping and Surface Coating Co-Free Ni-Rich Cathode*

Elemental modification has emerged as a pivotal strategy for tailoring the structural and electrochemical performance of Ni-rich layered oxide cathodes. Through deliberate doping, key parameters such as lattice oxygen coordination, cationic ordering, phase stability, charge/discharge capacity, working voltage, cycling durability, thermal stability, and gas evolution can be finely regulated, with outcomes strongly influenced by dopant type, concentration, and lattice substitution site.[87] Both cationic and anionic dopants have been explored extensively: cations spanning monovalent to hexavalent states (e.g., Na^+, Mg^{2+}, Sr^{2+}, Ca^{2+}, Ba^{2+}, Al^{3+}, Fe^{3+}, Cr^{3+}, Y^{3+}, La^{3+}, Ga^{3+}, Eu^{3+}, Ru^{4+}, Ti^{4+}, Zr^{4+}, Ce^{4+}, V^{5+}, Nb^{5+}, Ta^{5+}, Mo^{6+}, W^{6+}) and anions with diverse valences (F^-, Cl^-, Br^-, I^-, S^{2-}, Se^{2-}, B^{3-}, N^{3-}, P^{3-}) have

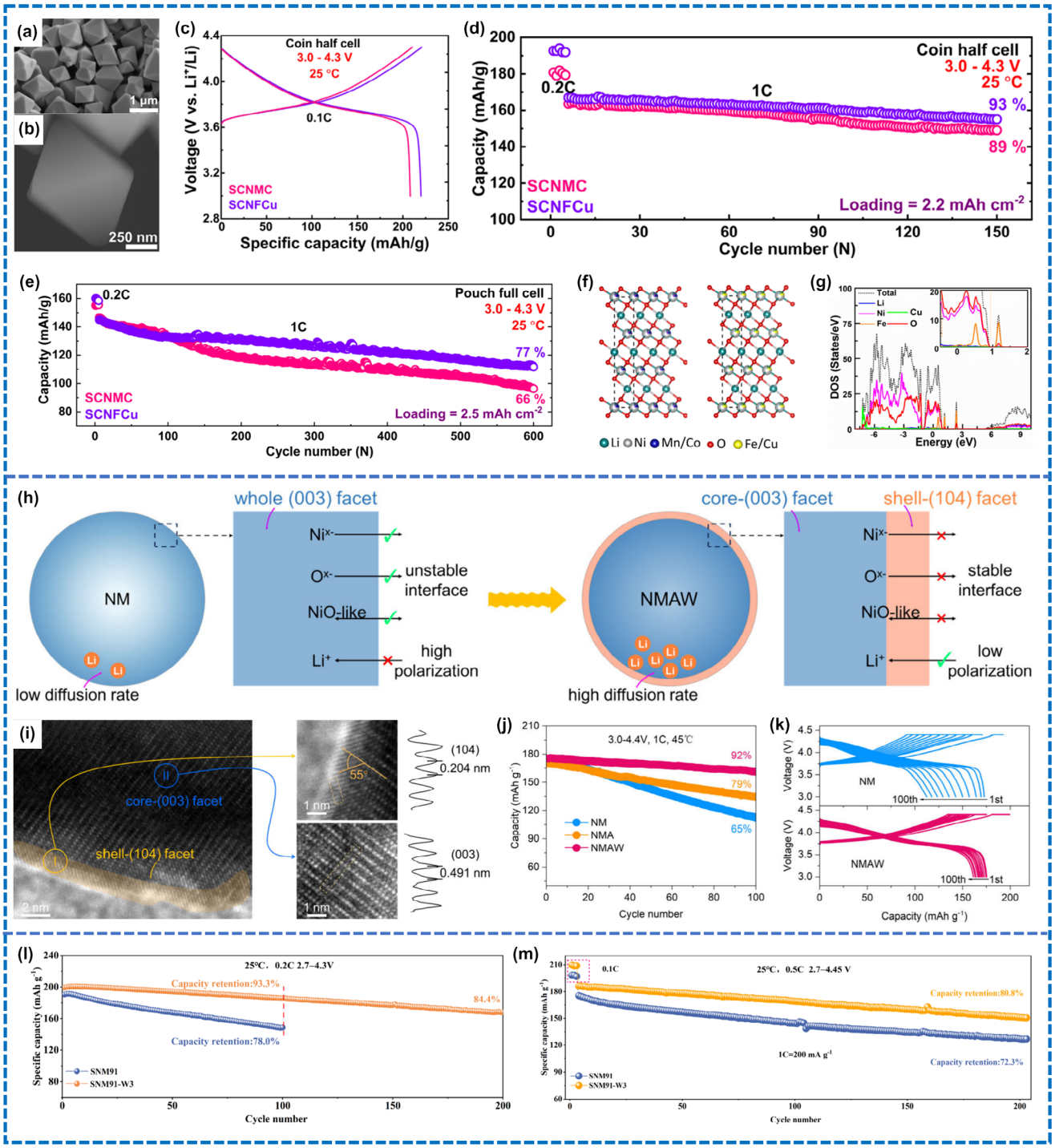

Figure 6. a, b) SEM images of SCNFCu cathodes, illustrating distinct morphological architectures. c) Galvanostatic charge–discharge curves at 0.1 C. d) cycling performance at 1 C. e) long-term cycling behavior in a pouch-type full cell. DFT calculations of f) crystal structure and g) density of states plots of SCNFCu. a–g) were reproduced with permission.[79] Copyright 2024 American Chemical Society. h) Structure characterization of the as-synthesized materials of $LiNi_{0.718}Mn_{0.271}Al_{0.010}W_{0.001}O_2$. i) HRTEM images of NMAW. j) Cycling performance of NM, NMA, and NMAW at 1 C under 45 °C, k) Charge and discharge curves of NM and NMAW at different cycle numbers at 1 C under 45 °C. h-k) were reproduced with permission.[24] Copyright 2024 American Chemical Society. l) Cycling performance of SNM91 and SNM91-W3 at different cycles, m) Cycling performance of full cell at 0.5 C within the voltage range of 2.7–4.45 V. l–m) were reproduced with permission.[86] Copyright 2025 Elsevier.

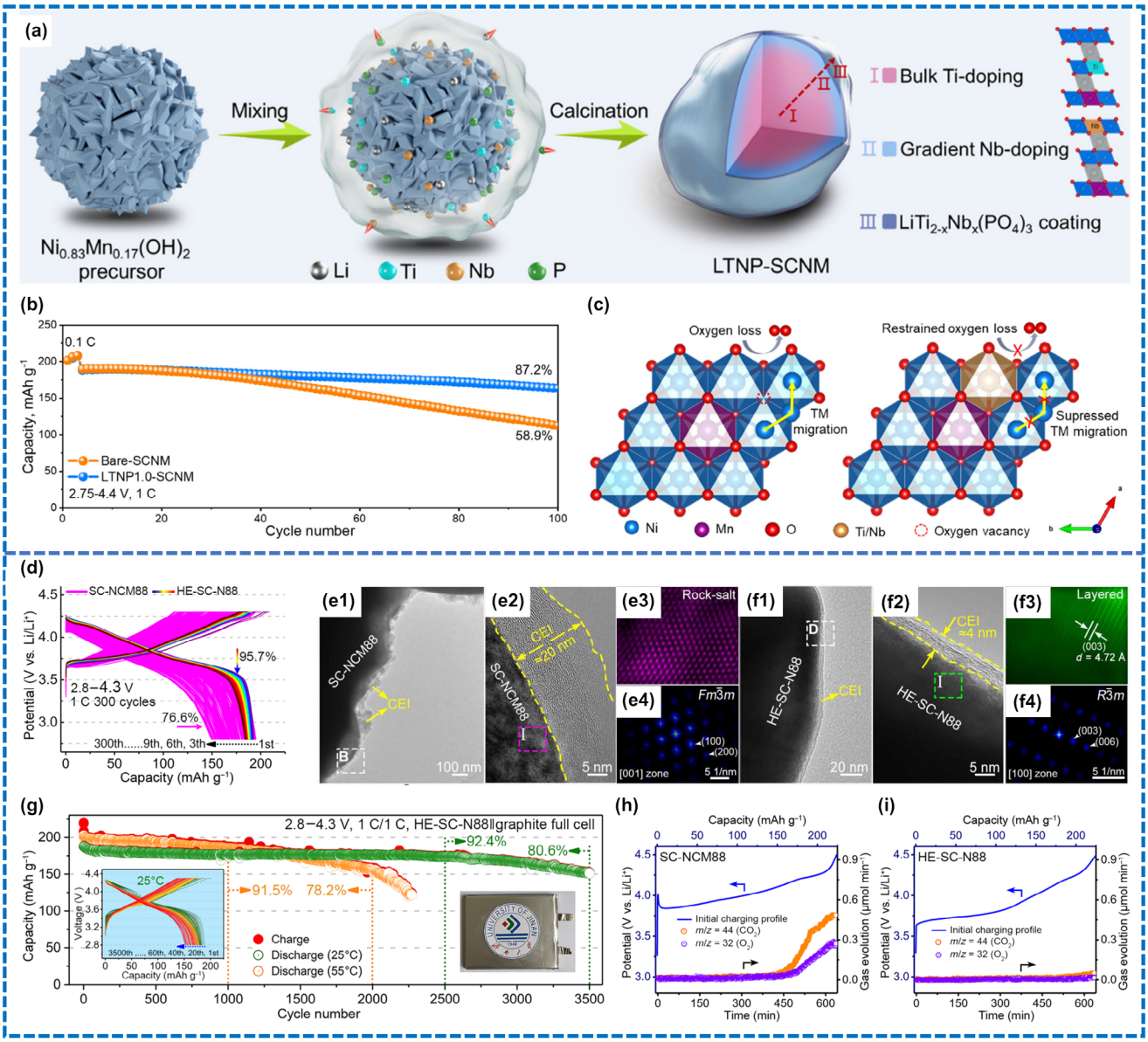

Figure 7. a) Schematic illustration of the LTNP-SCNM synthesis process. b) Cycling performance of bare-SCNM and LTNP1.0-SCNM at 1 C for 100 cycles. c) The lattice oxygen release and Ni^{2+} migration configurations during high-voltage cycling. a–c) were reproduced with permission.[101] Copyright 2024 Elsevier. d) Charge–discharge profiles of half cells measured between 2.8 and 4.3 V. e1–e4) STEM-HAADF images, magnified views, and FFT patterns of SC-NCM88. f1–f4) STEM-HAADF images, magnified regions, and FFT analyses of HE-SC-N88. g) Cycling stability in full cells at 1 C under 25 and 55 °C and corresponding voltage profiles and digital photo (insets), In situ DEMS spectra of h) SC-NCM88 and i) HE-SCN88 during the first charge. d–i) were reproduced with permission.[42] Copyright 2024 Science Advances.

been implemented, along with co-doping approaches, to enhance lithium storage properties.[88–90] The choice of substitution site—Li, TM, or oxygen—further allows precise control over lattice structure and redox behavior.[91]

Recent advances in surface engineering have highlighted several key coating materials for enhancing the stability and performance of single crystal CFNR cathodes, including Li_2MoO_4,[92] $Li_{1.25}Al_{0.25}Ti_{1.5}O_4$ (LATO),[93] $Li_{1.3}In_{0.3}Ti_{1.7}(PO_4)_3$ (LITP),[94] $TiBO_3$,[95] and $Li_{1.8}Sc_{0.8}Ti_{1.2}(PO_4)_3$ (LSTP).[96] Each of these coatings provides unique functionalities that address specific degradation mechanisms inherent to high-Ni, cobalt-free layered oxides. Li_2MoO_4 forms in situ conformal nanolayers from residual lithium, producing chemically coherent, ion-permeable interfaces that suppress electrolyte decomposition while maintaining efficient Li^+ transport. LATO coatings serve as mechanical reinforcements, mitigating planar gliding and preserving particle integrity during repeated cycling. LITP layers enrich the cathode surface with lithium ions, alleviating diffusion-induced stress and minimizing fracture in single-crystal particles. $TiBO_3$, with its intrinsic phase compatibility, reduces lattice mismatch and stabilizes the layered structure over extended cycling. LSTP combines high ionic conductivity with robust

interfacial stability, enabling reliable operation at voltages up to 4.6 V and supporting long-term cyclability. The integration of these coatings with targeted elemental doping provides a synergistic approach to address both bulk and surface challenges in Co-free Ni-rich cathodes. Doping and surface modification together enhance structural stability by suppressing TM migration, planar gliding, and lattice strain.[97,98] They improve Li^+ transport through high-Li-content surfaces and vacancy-mediated diffusion pathways, while simultaneously providing interfacial protection against electrolyte-induced side reactions, oxygen evolution, and formation of electrochemically inactive rock-salt phases.[59,99] These strategies collectively enhance cycling durability by mitigating mechanical fracture and stabilizing phase transitions and enable safe high-voltage operation through optimized lattice chemistry and interfacial robustness.[100] Such a combined approach underscores the critical role of advanced doping and surface coatings in unlocking the full electrochemical potential of Co-free Ni-rich single-crystal cathodes, paving the way for high-energy, long-lasting LIB applications.

Deng et al. demonstrated that Co-free single-crystal $LiNi_{0.83}Mn_{0.17}O_2$ (SCNM) exhibits markedly improved cycling stability through bulk Ti doping, gradient Nb doping and the $LiTi_{2-x}Nb_x(PO_4)_3$ (LTNP) surface coating as shown in **Figure 7**a.[101] This integrated strategy delivers an initial discharge capacity of 205.8 mA h g^{-1} at 0.1 C and superior cycling stability with 87.2% retention after 100 cycles at 1 C, compared to the bare SCNM (Figure 7 b). Bader charge analysis confirmed that Ti and Nb strengthened the metal-oxygen bonding network, restrained oxygen loss, and suppressed transition-metal migration, thereby preserving structural integrity as depicted Figure 7c.[42] Liang et al. addressed the long-standing instability of CFNR by combining single-crystal morphology with high-entropy doping to yield $LiNi_{0.88}Mn_{0.03}Mg_{0.02}Fe_{0.02}Ti_{0.02}Mo_{0.02}Nb_{0.01}O_2$ (HE-SC-N88).[42] Conventional SC-NCM88 retained only 76.6% of its capacity after 300 cycles, whereas HE-SC-N88 maintained 95.7% (Figure 7d). Microscopy, HR-TEM revealed that SC-NCM88 developed a thick (~20 nm), unstable CEI layer and surface rock-salt reconstruction (Figure 7e1–e4), while HE-SC-N88 preserved a thin (~4 nm) CEI and ordered lattice fringes (Figure 7f1–f4). The authors evaluated full-cell configurations with graphite anodes and demonstrated that HE-SC-N88 exhibited remarkable cycling durability, retaining 92.4% of its initial capacity after 2500 cycles at 25 °C and 80.6% after 3500 cycles, while at 55 °C the capacity retention remained above 78.2% after 2000 cycles, as illustrated in Figure 7h. Gas analysis revealed severe O_2 and CO_2 release in SC-NCM88 (Figure 7h), while HE-SC-N88 generated minimal gases (Figure 7i), confirming suppressed oxygen escape and electrolyte decomposition. These strategies collectively restrained oxygen instability, mitigated interfacial degradation, and enabled long-term high-voltage cycling with improved safety. **Table 1** summarized the synthesis strategies and electrochemical performance of Co-free Ni-rich single crystals reported across prior studies.[21,24,42,63,65,70,71,73,74,79,86,101–112]

The pursuit of CFNR single-crystal cathodes is driven by both sustainability and performance requirements for advanced LIBs. Their importance can be outlined as follows: 1) the reduction of cobalt dependence addresses issues of limited supply, cost fluctuations, and ethical concerns, 2) Ni-rich layered oxides provide the high capacity and energy density needed for large-scale applications such as EVs and stationary storage, 3) single-crystal morphologies minimize intergranular cracking and surface degradation, thereby extending cycle life under practical operating conditions, 4) controlled elemental substitution and high-entropy design strategies enhance lattice stability, suppress oxygen evolution, and reduce Li/Ni disorder, 5) surface and interface engineering improve resistance to electrolyte attack, promote uniform Li^+ transport, and support stable operation at high voltages, and 6) scalable synthesis methods, particularly co-precipitation and molten salt approaches, enable the production of structurally robust single-crystal particles suitable for commercialization. Collectively, these advancements establish CFNR single-crystal cathodes as strong candidates for the next generation of durable, high-energy, and sustainable LIBs.

2.6. Cobalt-Free Spinel Type Single Crystal Cathodes

Spinel oxides with the general formula $LiMn_2O_4$ were first proposed as cathode materials for LIBs by Michael Thackeray in the early 1980s.[113] Compared to other oxide cathode materials, $LiMn_2O_4$ offers several advantages, including low cost, environmental benignity, and enhanced safety.[114,115] Its unique MnO_2 framework enables a three-dimensional (3D) lithium-ion diffusion pathway, contributing to its superior rate capability.[116] In the spinel structure of $LiMn_2O_4$, Mn occupies the 16d octahedral sites, while Li resides in the 8a tetrahedral sites within a cubic close-packed oxygen lattice, as illustrated in **Figure 8**a.[117] The robust edge-sharing Mn_2O_4 octahedral framework forms a network of intersecting tunnels via face-sharing between tetrahedral lithium (8a) sites and empty octahedral (16c) sites, enabling fast 3D lithium-ion diffusion.[117] Despite excellent rate performance afforded by the 3D diffusion pathways, $LiMn_2O_4$ suffers from significant capacity fading at elevated temperatures.[118] Two primary degradation mechanisms have been proposed to explain this capacity degradation: 1) Mn^{2+} dissolution into the electrolyte, driven by proton-induced corrosion (Figure 8b), and 2) irreversible structural transformation from the spinel to a tetragonal phase, primarily due to the Jahn–Teller (J-T) distortion associated with Mn^{3+} ions (Figure 8c), along with the development of micro-strain (Figure 8d).[117,119] Mn dissolution is typically attributed to the disproportionation reaction:

$$2\ Mn^{3+} \rightarrow Mn^{4+} + Mn^{2+} \quad (1)$$

While $LiMn_2O_4$ is a cost-effective and safer alternative to other cathode materials, it exhibits relatively lower practical capacity and energy density. To address Mn dissolution and capacity fading, various strategies have been explored, focusing on structural stabilization and suppression of Mn^{2+} leaching. One effective approach is the synthesis of single crystal morphologies, which help prevent particle cracking by ensuring uniform lattice expansion/contraction and minimizing phase boundaries.[120] For example, Akimoto et al. reported the synthesis of octahedral-shaped single-crystal $LiMn_2O_4$ and $LiM_xMn_{2-x}O_4$ (M = Cr, Co, Ni) in 2001 and 2003, respectively. These crystals, approximately 0.09 × 0.09 × 0.09 and 0.2 × 0.2 × 0.2 mm^3 in size (**Figure 9**a, b), were synthesized using solvent evaporation flux and high-temperature molten chlorides methods at 1023 K, respectively.[121,122] In 2008, Hosono et al. synthesized single-crystal $LiMn_2O_4$ nanowires using $Na_{0.44}MnO_2$ nanowires as a self-template for sodium/lithium ion exchange.[123] SEM images (Figure 9c) showed well-retained nanowire morphology after heat treatment at 800 °C for 12 hours. As far as electrochemical performance is concerned, the prepared sample exhibits much improved electrochemical cycling performance compared to the commercial powder supplied and produced by other companies, as shown in Figure 9d,e. For instance, after 100 cycles at 5 A g^{-1}, a large

Table 1. Summary of electrochemical properties of single-crystal Co-free Ni-rich cathodes, emphasizing capacity retention and stability under voltage operation.

Single crystal Co-free Ni-rich cathode materials	Description	Synthesis method	Discharge capacity (mA h g^{-1})/C-rate	Capacity retention (%)/cycle number	References
$LiNi_{0.8}Mn_{0.18}Fe_{0.02}O_2$	A single-crystal Co-free composition was reported to enhance voltage response and stability. Fe incorporation strengthened the mid-voltage plateau, while Mn suppressed oxygen release and stabilized the lattice. Operando studies confirmed a reversible H2–H3 transition with reduced strain, delivering long cycling stability	Co-precipitation	208.4/0.1 (3.0–4.35 V)	84/1000	[21]
$LiNi_{0.718}Mn_{0.271}Al_{0.010}W_{0.001}O_2$	Dual Al/W substitution in single-crystals produced a core-shell structure with dominant (104) facets. These facets facilitated Li^+ transport and reduced interfacial polarization, while bulk Al improved lattice integrity, suppressing interfacial degradation	Co-precipitation	189.1/0.1 (3.0–4.4 V)	92/100	[24]
$LiNi_{0.88}Mn_{0.03}Mg_{0.02}Fe_{0.02}Ti_{0.02}Mo_{0.02}Nb_{0.01}O_2$	High-entropy doping in single-crystals minimized lattice strain and grain-boundary stress. Multivalent dopants acted as structural pillars, suppressing oxygen release, phase instability, and thermal degradation, yielding improved stability under harsh cycling	Co-precipitation	210/0.1 (2.8–4.3 V)	81.2/400 (2.8–4.5 V)	[42]
$LiNiO_2$	Single-crystal-like $LiNiO_2$ preserved particle integrity and resisted microcracking compared to its polycrystalline analogue, enabling improved structural stability and longer cycling durability	Co-precipitation	241/0.1 (2.5–4.3 V)	63.5/500	[63]
$LiNi_{0.95}Mn_{0.05}O_2$	Well-defined single-crystal particles with truncated octahedral morphology eliminated grain boundaries. The exposure of (010) facets enhanced Li^+ diffusion and maintained structural order, suppressing surface degradation	Co-precipitation	218.2/0.1 (2.8–4.5 V)	84.4/200	[65]
$LiNi_{0.6}Mn_{0.4}O_2$	Moderate Li/Ni mixing in single-crystal NM64 reduced anisotropic lattice contraction and suppressed crack formation, ensuring higher mechanical and thermal stability than Ni-richer NM82	Co-precipitation	185.9/0.5 (2.7–4.6 V)	75.2/200	[70]
$LiNi_{0.6}Mn_{0.4}O_2$	Single-crystal NM64 displayed a crack-resistant morphology with a well-ordered layered framework, enabling low-cost, cobalt-free cathodes with superior thermal robustness	Co-precipitation	209.7/0.2 (2.6–4.5 V)	54.8/200	[71]
$LiNi_{0.75}Mn_{0.25}O_2$	Single-crystals synthesized without Co developed lithium-rich nanodomains that induced lattice strain and irreversible degradation. Voltage fading occurred due to localized instability despite improved safety	Co-precipitation	194/0.1 (2.8–4.6 V)	85/100	[73]
$LiNi_{0.9}Mn_{0.1}O_2$	Single-crystal SC-NM91 suppressed grain-boundary cracking and limited Li/Ni disorder. The dense lattice resisted layered to rock-salt transformations, reducing CEI growth and interfacial side reactions	Co-precipitation	200/0.1 (3.0–4.3 V)	85.72/300	[74]
$LiNi_{0.94}Fe_{0.05}Cu_{0.01}O_2$	A Mn/Co-free single-crystal with Fe/Cu substitution demonstrated improved mechanical robustness and suppressed dissolution. The architecture preserved interface stability while maintaining cost efficiency	Co-precipitation	220/0.1 (3.0–4.3 V)	93/150	[79]
W doped $LiNi_{0.9}Mn_{0.1}O_2$	Uniform W incorporation via two-step sintering enhanced Li^+ diffusion and electronic conductivity. Strong W–O bonds reinforced lattice stability, suppressing oxygen release and phase degradation	Co-precipitation	207/0.1 (3.0–4.3 V)	84.4/200	[86]
Ti/Nb doped and $LiTi_{2-x}Nb_x(PO_4)_3$ coated $LiNi_{1-x}Mn_xO_2$	A dual strategy of Ti/Nb bulk doping and surface coating stabilized the layered structure. Doping suppressed oxygen release and migration, while the coated layer promoted robust CEI formation	Co-precipitation	205.8/1 (2.75–4.4 V)	87.2/100	[101]
$LiNi_{0.95}Mn_{0.05}O_2$	Solid-state synthesis of single-crystal NM9505 produced a thermodynamically stable layered structure. Proton removal and uniform Li insertion enabled quasi-equilibrium phase evolution	Co-precipitation	210/0.1 (2.8–4.5 V)	–	[102]

Table 1. Continued

Single crystal Co-free Ni-rich cathode materials	Description	Synthesis method	Discharge capacity (mA h g^{-1})/C-rate	Capacity retention (%)/cycle number	References
$LiNi_{0.9}Mn_{0.05}Al_{0.05}O_2$	PVP-assisted synthesis produced single-crystals with reduced Li/Ni mixing and dense morphology. The architecture resisted cracking and enhanced phase reversibility during cycling	Hydrothermal	205/0.1 (2.8–4.4 V)	93.4/100	[103]
$LiNi_{0.8}Mn_{0.2}O_2$	Co-free NM suffered from severe antisite defects, strong H2-H3 transitions, and lattice distortion. Although structurally unstable, it exhibited enhanced safety benefits over Co-containing analogues	Co-precipitation	184.3/0.2 (2.95–4.3 V)	82/100	[104]
$LiNi_{0.8}Mn_{0.16}Al_{0.04}O_2$	A one-step chelation-assisted method produced crack-free single-crystals. Al incorporation suppressed cation mixing and improved ion transport, enhancing rate capability and scalability	Sol–Gel	204.1/0.1 (3.0–4.3 V)	82.1/100	[105]
Y/W doped $LiNi_{0.9}Mn_{0.1}O_2$	Dual Y^{3+}/W^{6+} doping reduced Li/Ni disorder and stabilized the layered framework. Improved lithium-ion diffusion and suppressed interfacial reactions enhanced cycle life and rate performance	Co-precipitation	204.1/0.1 (3.0–4.3 V)	82.1/100	[106]
$LiBO_2$ coating and B doped $LiNi_{0.75}Mn_{0.25}O_2$	Boron incorporation and $LiBO_2$ coating stabilized the structure by suppressing c-axis contraction, reducing oxygen activity, and limiting cracking. The dual strategy preserved H2-H3 transitions	Co-precipitation	199.7/0.1 (2.7–4.5 V)	90.3/100	[107]
$LiNi_{0.8}Mn_{0.2}O_2$	Submicron single-crystals prepared via jet milling displayed dense, uniform particles with suppressed microcracking, reduced Li/Ni disorder, and enhanced diffusion kinetics	Co-precipitation	206.1/0.1 (2.75–4.3 V)	–	[108]
W/Zr doped $LiNi_{0.75}Mn_{0.25}O$	High-temperature doping incorporated W/Zr into the lattice. Zr reduced cation mixing and polarization, improving ion mobility, while W contributed marginal structural benefits	Co-precipitation	185.2/0.1 (3.0–4.3 V)	90/200	[109]
$LiNi_{0.9}Mn_{0.1}O_2$	Single-crystals of SNM9–3 with well-aligned (010) facets resisted cracking and cation mixing, supporting improved stability during extended cycling	Co-precipitation	204.1/0.1 (3.0–4.3 V)	72.1/100	[110]
$LiNi_{0.83}Co_{0.10}Mn_{0.07}O_2$	Crack-free single-crystals reduced intergranular fractures, maintained morphology, and resisted dissolution. They exhibited improved phase reversibility compared with polycrystalline analogues	Co-precipitation	193.4/0.1 (2.7–4.5 V)	84.8/400	[111]
Mg/Nb/Al co-doped $LiNi_{0.9}Mn_{0.1}O_2$	High-entropy co-doping and surface layer formation stabilized oxygen reversibility and lattice integrity. The interfacial coating formed a robust CEI, mitigating HF corrosion and enhancing longevity	Co-precipitation	213/0.1 (2.7–4.3 V)	90.1/300	[112]

capacity of around 100 mA h g^{-1} was still maintained, outperforming the other commercially available $LiMn_2O_4$ materials. Various single-crystal morphologies of $LiMn_2O_4$, including nanorods, nanowires, and nanotubes, have since been reported.[124–128] Sun et al. synthesized single-crystal $LiMn_2O_4$ with different dimensionalities by tailoring the morphology of the MnO_2 precursor (Figure 9f).[129] SEM images (Figure 9g) revealed 1-D nanorods (top two images; average diameter ~100 nm and length of about 1.6 μm), 2-D nanoplates (middle two images; diameter of 300–400 nm and a thickness of 20 nm), and 3-D octahedral particles (bottom two; edge length of about 1 μm). Among them, the 1-D nanorods exhibited the best electrochemical performance in terms of long-term cycling at 0.1 C, as shown in Figure 9h. Likewise, Lin et al. developed a porous $LiMn_2O_4$ architecture composed of single-crystalline nanoparticles using $MnCO_3$ cubes as precursors.[130] After heat treatment at 600 °C, $MnCO_3$ decomposed into porous Mn_2O_3 cubes, which subsequently reacted with a lithium precursor to form spinel $LiMn_2O_4$. SEM images of as synthesized $MnCO_3$ precursor are presented in Figure 9i1,i2, while Figure 9i3,i4 represents the thermal decomposition of $MnCO_3$, resulting in the formation of Mn_2O_3, which in turns reacted with Li salt to form porous cubes (average edge of 250 nm) with $LiMn_2O_4$ single crystalline particles (~50 nm), as presented in SEM, tem and HR-TEM images in Figure 9j1–j6. A schematic formation mechanism is illustrated in Figure 9k. A deep cycling performance was elaborated by the prepared nanostructure up to 4100 cycles at 10.0 C rate maintaining a capacity retention of 80.55%, as shown in Figure 9l. Apart from adopting elegant nanostructure

Figure 8. a) Crystal structure of $LiMn_2O_4$ along with the Li^+ 8a-16c-8a diffusion pathways. b) Mn disproportionation reaction mechanism. c) Molecular orbital energy diagram of MnO_6 and 3d orbitals of Mn^{2+}/Mn^{4+} and high/low spin Mn^{3+} ions along with the illustration of change in MnO_6 that undergoes the Jahn–Teller distortion. d) Schematic illustration of the irreversible phase of $LiMn_2O_4$ accelerating the dissolution of Mn as surface cracks expand during the cycling thus forming a vicious cycle. a–d) were reproduced with permission.[117] Copyright 2025, Wiley.

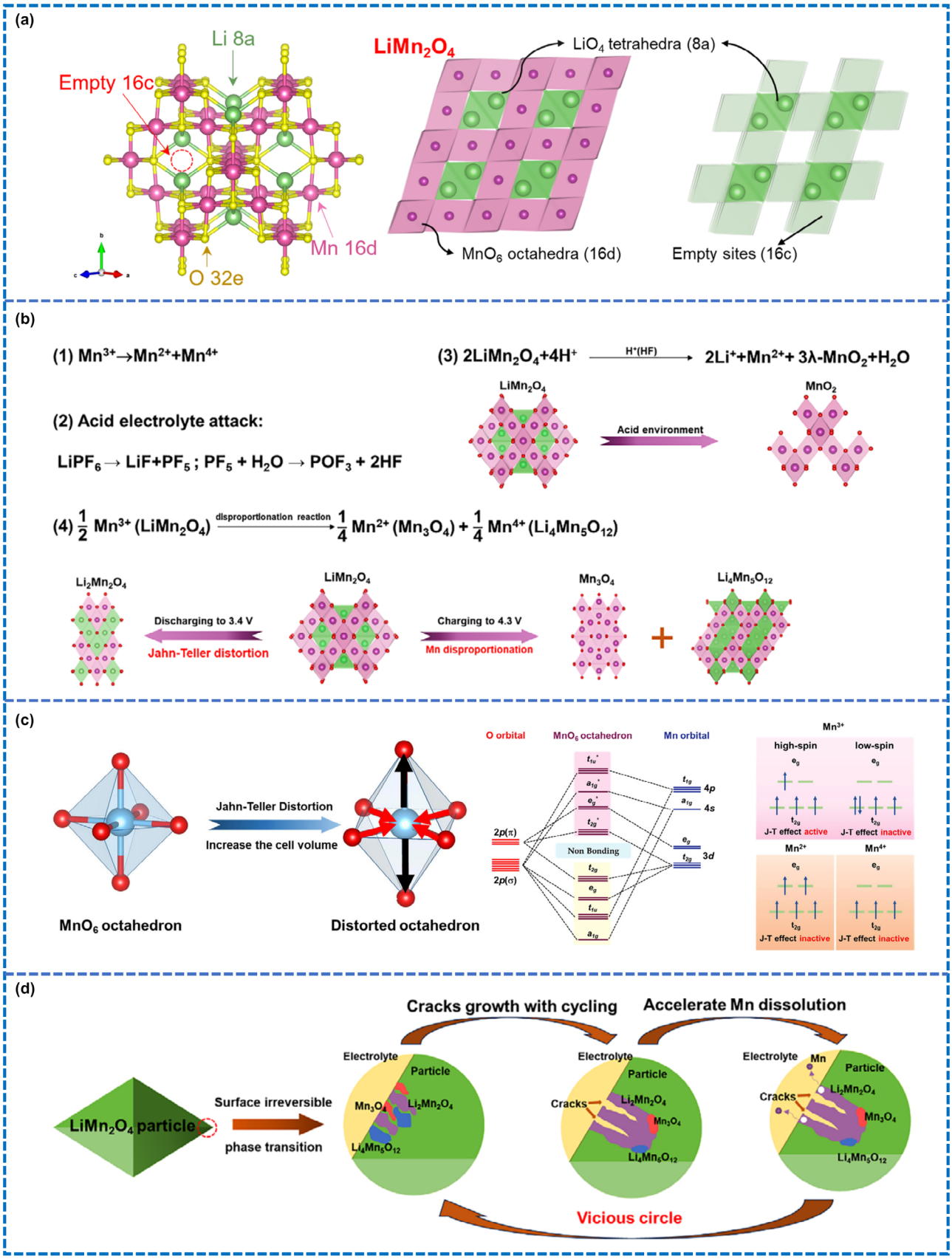

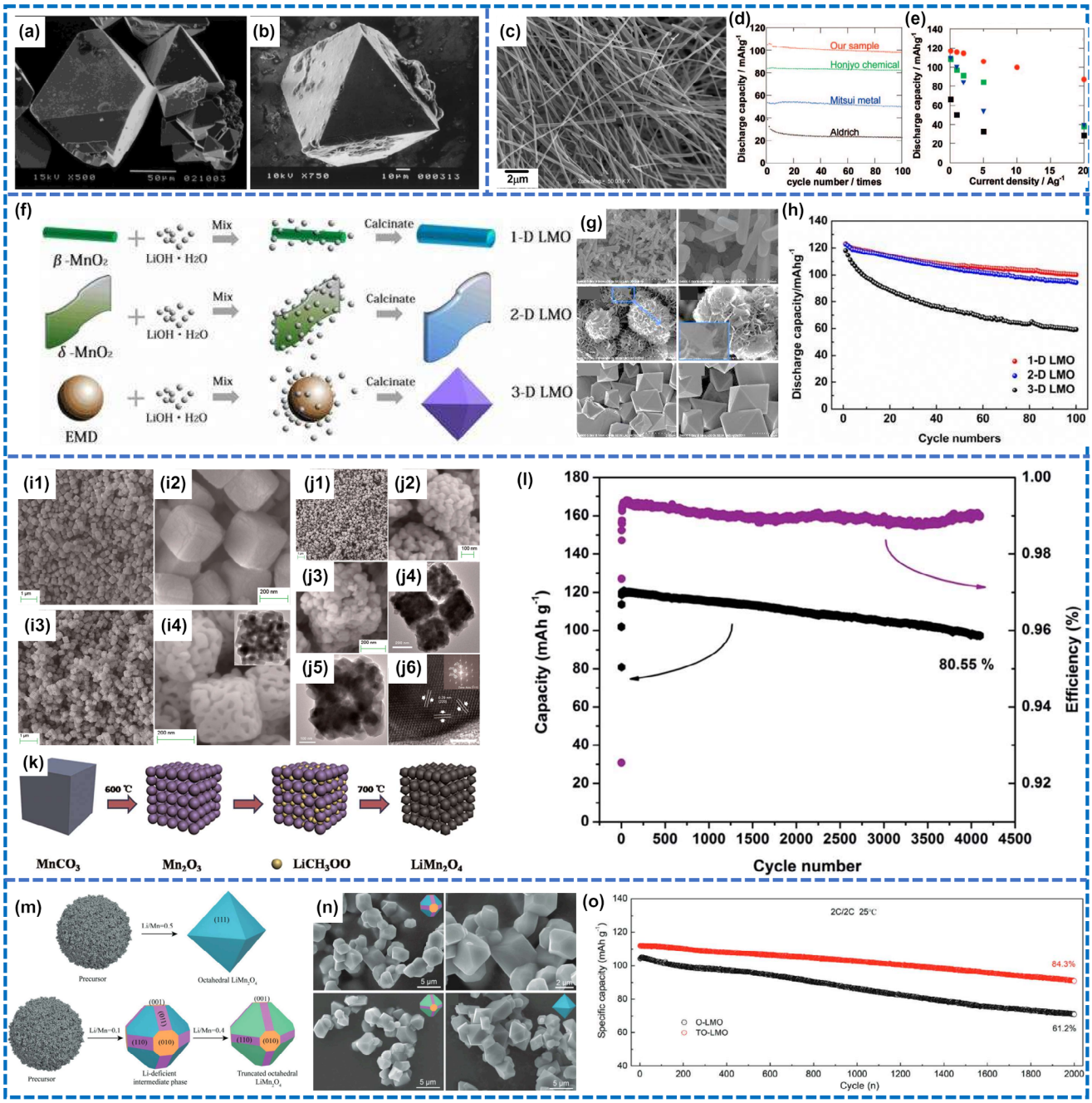

Figure 9. SEM image of an octahedral-shaped single crystal of a) $LiMn_2O_4$ and b) $LiM_xMn_{2-x}O_4$ (M = Cr, Co, Ni).[121,122] Copyright 2001, Elsevier. Copyright 2003, American Chemical Society. c) SEM image of the single crystalline $LiMn_2O_4$ nanowires. d, e) Cycling performance comparison of single crystalline $LiMn_2O_4$ nanowires at 5 A g^{-1} along with other commercially available $LiMn_2O_4$ materials. c–e) were reproduced with permission.[123] Copyright 2008, American Chemical Society. f) Schematic illustration of the formation mechanism of 1-D, 2-D, and 3-D single crystalline $LiMn_2O_4$ samples. g) FE-SEM images of 1-D nanorods (top two images), 2-D nanoplates (middle two images), and 3-D octahedral single crystalline particles (bottom two). h) Cycling performance at a current density of 0.1 C-rate between 3.0 and 3.4 V. f–h) were reproduced with permission.[129] Copyright 2014, Elsevier. i1, i2) SEM images of $MnCO_3$ precursor. i3, i4) SEM images of Mn_2O_3 formed by thermal decomposition of $MnCO_3$. j1–j6) SEM, TEM and HR-TEM images of the porous cubes with single crystalline $LiMn_2O_4$ particles. k) Schematic illustration of the formation process. l) Long-term cycling performance at 10.0 C. i1–l) were reproduced with permission.[130] Copyright 2014, Royal Society of Chemistry. m) Schematic diagram of the octahedral (O) $LiMn_2O_4$ exposed with (111) facet and truncated octahedral (TO) $LiMn_2O_4$ exposed with (111), (100), and (110) facets. n) SEM images of the intermediate phase (top two), TO (left bottom), and O (right bottom). o) Long-term cycling stability at a current rate of 2.0 C. m–o) were reproduced with permission.[135] Copyright 2023, Advanced Science.

Table 2. Electrochemical performance comparison of single crystal spinel-type $LiMn_2O_4$ cathodes.

Single crystal material	Brief description	Synthesis method	Discharge capacity (mA h g^{-1})/ C-rate	Capacity retention (%)/ cycle Number	References
$LiMn_2O_4$	High-quality single crystalline cubic spinel nanowires were synthesized using a self-template strategy, which display high rate capability performance (even at 20 A g^{-1}) with flat charge–discharge plateaus	Hydrothermal/ ion-exchange	108/5.0[a]	92/100	[123]
$LiMn_2O_4$	Single-crystalline -MnO_2 nanorods were synthesized using hydrothermal method and chemically converted to $LiMn_2O_4$, which reveals high charge storage capacity even at high power rates.	Co-precipitation	100/1.0	85/100	[124]
$LiMn_2O_4$	Hydrothermal method was used to synthesize single crystalline cubic spinel $LiMn_2O_4$ nanowires and their electrochemical performance were tested in an aqueous $LiNO_3$ solution.	Hydrothermal	110/10.0	65/130	[125]
Al-doped $LiMn_2O_4$	To improve the long-term cycling stability at elevated temperature along with the efficient suppression of Jahn–Teller distortion and Mn dissolution, Al-doped single-crystalline nanotubes of $LiMn_2O_4$ were synthesized using Co-precipitation.	Co-precipitation	90/5.0	80/800	[126]
$LiMn_2O_4$	A chemically transformed from [001]-oriented -MnO_2 template to [110]-oriented $LiMn_2O_4$ was synthesized via a template-engaged reaction. The prepared powder demonstrated prolonged charge–discharge cycling at a relatively high current density.	Hydrothermal	90/5.0	70/1500	[127]
$LiMn_2O_4$	Tetragonal -MnO_2 as a starting material was utilized to synthesized single crystalline $LiMn_2O_4$ nanorods with a diameter ~ 100 nm. The obtained powder exhibit superior high-rate capability and good cycling stability.	Hydrothermal	95/3.0	75/500	[128]
$LiMn_2O_4$	A single crystalline $LiMn_2O_4$ film with an atomically flat surface by solid-state reaction from a MnO wafer with $LiOH.H_2O$ wafer.	Solid-State	116/0.3	-	[198]
$LiMn_2O_4$	Single-crystalline $LiMn_2O_4$ with different dimensional nanostructures were prepared and their electrochemical performance was compared, which reveals 1-D $LiMn_2O_4$ exhibits the best electrochemical performance.	Hydrothermal	123/0.1	81/100	[129]
$LiMn_2O_4$	Porous $LiMn_2O_4$ was fabricated with cubic $MnCO_3$ as precursor and characterized in terms of structure and performance as the cathode of a lithium battery.	Co-precipitation	120/10.0	81/4000	[130]
$LiMn_2O_4$	A two-step approach was employed to prepare well-shaped octahedral Mn_3O_4 initially and then transferred to $LiMn_2O_4$ by the solid state lithiation process. The octahedral particles demonstrated superior electrochemical properties in comparison with the particles prepared via sol–gel.	Hydrothermal	123/1.0	85/200	[199]
$LiMn_2O_4$	Single-crystalline $LiMn_2O_4$ nanorods were successfully synthesized via a simple, low-cost and eco-friendly approach which further reveals excellent electrochemical performance.	Hydrothermal	123/1.0	89/100	[200]
C-coated $LiMn_2O_4$	Carbon-coated single-crystal $LiMn_2O_4$ nanowires were obtained via a high-temperature solid-state method under air environment, which delivers large capacity and long-term cycling stability.	Solid-State	114/1.0	90/500	[201]
Al-F co-doped $LiMn_2O_4$	A pure phase $LiMn_2O_4$ is synthesized by a high-temperature solid-phase method along with the element-doping to improve the overall electrochemical performance.	Solid-State	111/0.1	80/382	[131]
$LiMn_{2-x}M_xO_4$ (M = Al, Fe, and Ni)	Facile synthesis approach to prepare single-crystalline spinel cathode by a control oxidative conditions during the lithiation process was adopted.	Solid-State	85/0.3	87/200	[132]
Al-doped $LiMn_2O_4$	Micrometer-sized and octahedral-shaped Mn_2O_3 single crystal doped with various elements (Al, Ti, Ni, and Zr) were prepared by an ethanothermal synthesis and employed as precursor for spinel cathodes.	Solid-State	103/0.3	90/200	[202]
$LiMn_2O_4$	Single-crystalline $LiMn_2O_4$ nanoparticles were synthesized through the gel combustion method assisted by microwave followed by calcination treatment. The prepared material display exceptional electrochemical performances including good rate capability and better cycling stability.	Gel combustion/ Microwave	121/0.2	90/300	[203]
$LiMn_2O_4$	The synergistic effects of single crystals and the orientation of exposed crystal planes significantly reduce the disproportionation of Mn^{3+} ions and thereby improve structural integrity and hence, electrochemical performance.	Co-precipitation	112/2.0	84/2000	[135]

[a]A g^{-1}.

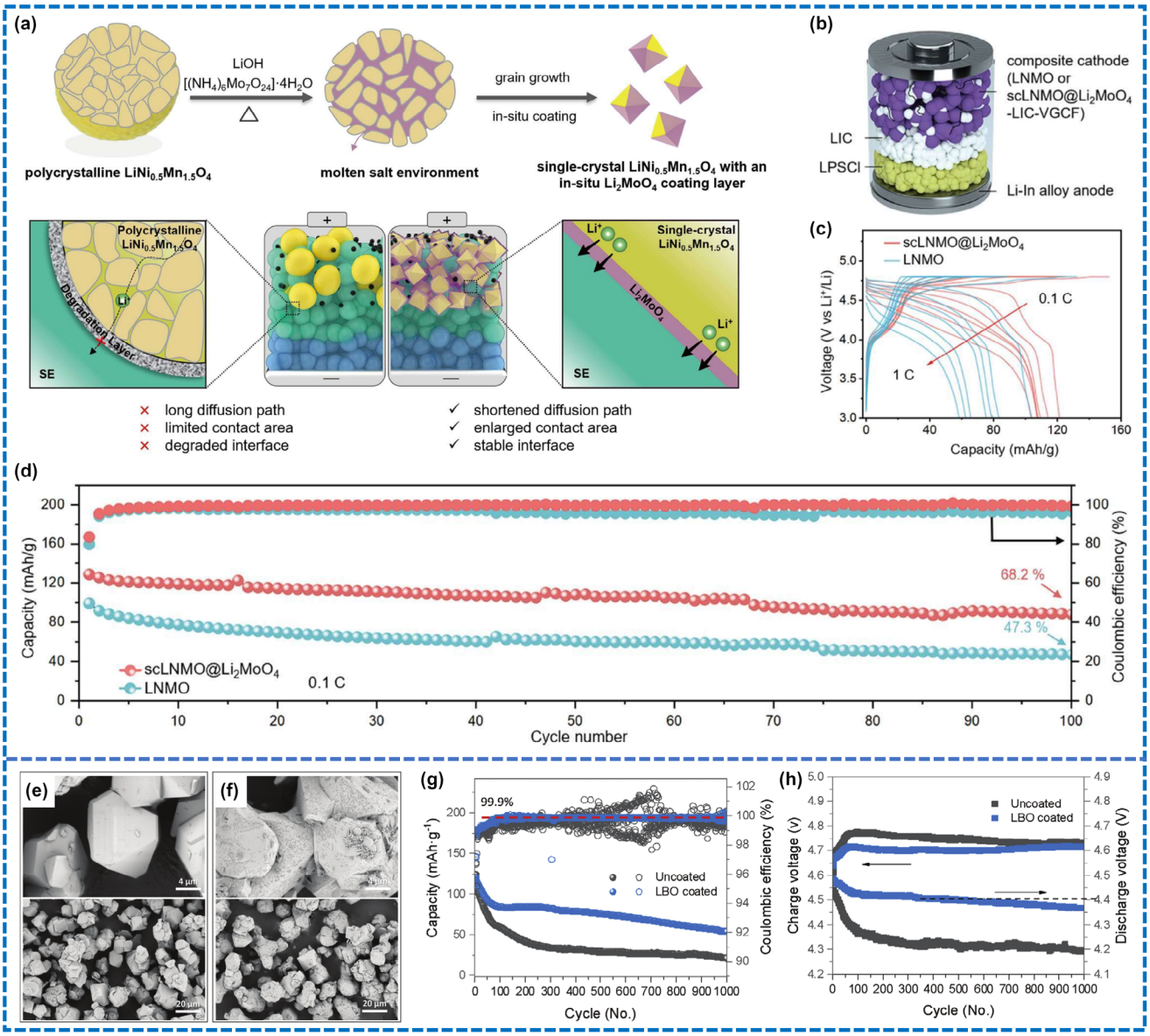

Figure 10. a) Schematic illustration of the molten salt annealing approach along with the in situ Li_2MoO_4 coating layer. b) Schematic diagram of the solid-state full cell. c) Charge/discharge curves at different current densities ranging from 0.1 to 1.0 C. d) long-term cycle performance comparison. a-d) were reproduced with permission[136] Copyright 2025, Science China Press 2025. e) Micrographs of uncoated LNMO. f) Micrographs of LBO-coated LNMO with respective large-scale view. g) Full-cell cycling performance comparison of uncoated and LBO-coated LNMO at 0.3 C rate. h) Corresponding average charge/discharge voltage. e–h) were reproduced with permission.[137] Copyright 2024, Wiley-VCH.

design strategy for $LiMn_2O_4$ single crystal, element doping is another effective approach to further improve the electrochemical performance. For instance, Li et al. prepared Al^{3+}/F^- co-doped spinel $LiMn_2O_4$ single-crystal and claim that the improvement in the material performance is primarily due to doping which inhibit Jahn–Teller distortion, alleviate the dissolution of Mn, and broadening Li^+ diffusion channels.[131] Similar studies were carried out by Park et al. by analyzing the effect of oxidative synthesis condition on the performance of single crystalline $LiMn_{2-x}M_xO_4$ (M = Al, Fe, and Ni) spinel cathodes.[132] Furthermore, Mn^{2+} dissolution in $LiMn_2O_4$ has been reported to be strongly dependent on the orientation of the exposed crystal planes.[133,134] Engineering the orientation of these exposed planes in spinel $LiMn_2O_4$ is thus proposed as an effective strategy to mitigate Mn^{2+} dissolution and improve the cycling stability. To exploit this, Hou et al. designed truncated octahedral single-crystal $LiMn_2O_4$ (TO-LMO) structures, mainly exposing (111) facets with partial truncation of (100) and (110) facets.[135] A schematic of the formation mechanism with both truncated octahedral and octahedral morphology is presented in Figure 9m. In the synthesis approach, an intermediate Li-deficient phase, exhibiting a truncated octahedral morphology formed first with exposed facets (Figure 9n; top two images), evolved into TO-LMO (Li/Mn = 0.4) and regular octahedral LMO (O-

LMO, Li/Mn = 0.5), as shown in Figure 9n (left bottom) and Figure 9n (right bottom), respectively. Electrochemical testing demonstrated that TO-LMO offered superior cycling stability, with 84% capacity retention after 2000 cycles at 2.0 C, as shown in Figure 9o. These findings clearly demonstrate that rational design of $LiMn_2O_4$ at the single-crystal level—through morphology engineering, doping, and facet control—can significantly improve the structural and electrochemical stability of this promising cathode material. A summary of previous studies on single-crystal $LiMn_2O_4$, including synthesis methods, morphology, doping strategies, and electrochemical performance, is presented in **Table 2**. Furthermore, our literature survey reveals that single-crystal LMO has yet to achieve its full potential in conventional Li-ion batteries- particularly in full-cell configurations, due to undesirable side reactions with carbonates-based liquid electrolytes at high voltages. These reactions lead to TM dissolution and rapid capacity fading, as previously discussed. Notably, only two studies have explored the practical application of Ni-substituted LMO ($LiNi_{0.5}Mn_{1.5}O_4$ (LNMO)), in full-cell setups. For instance, W. Luo et al. synthesized and utilized a Co-free, spinel-structured single-crystal LNMO in a high-energy-density all-solid-state lithium battery (ASSLB) system.[136] The authors converted commercially available polycrystalline LNMO powder into single-crystal particles using a molten salt strategy. To enhance interfacial stability, a Li-ion-conductive Li_2MoO_4 coating was applied in situ, as presented in **Figure 10**a. The all-solid-state full cell arrangement consisted of a composite cathode containing pristine LNMO and Li_2MoO_4-coated single-crystal LNMO, mixed with Li_3InCl_6 (LIC) and vapor grown carbon fiber (VGCF) in a mass ratio of 50:45:5. A Li-In alloy was used as the anode, and a LIC/$Li_{5.4}PS_{4.4}Cl_{1.6}$ (LPSCl) mixture served as the solid electrolyte, as shown in Figure 10b. Charge/discharge curves measured at current densities ranging from 0.1 to 1.0 C demonstrate that the coated single-crystal LNMO consistently delivers higher capacities (Figure 10c). Specifically, the capacity decreased from 121.3 to 103.6 mA h g^{-1} with a tenfold increase in current, corresponding to an 85% capacity retention. In contrast, pristine LNMO showed a drop from 103.4 to 59.4 mA h g^{-1}, retaining only 57% of its initial capacity. Regarding long-term cycling stability, the coated LNMO maintained a discharge capacity of 87.9 mA h g^{-1} after 100 cycles at 0.1 C, equating to a 68.2% retention (Figure 10d). Meanwhile, pristine LNMO retained only 47.3%, with a final capacity of 46.9 mA h g^{-1}. The authors attributed the improved electrochemical performance to the Li_2MoO_4 coating, which stabilized the electrode–electrolyte interface and suppressed parasitic side reactions. Similarly, Park et al. investigated the effect of lithium borate ($LiBO_2$) as the surface coating on the electrochemical performance of commercially available LNMO single crystals in a full cell arrangement.[137] As presented in Figure 10e, the uncoated LNMO displayed a uniform light gray color and a particle size of approximately 6–8 μm, consistent with typical single-crystal morphology. In contrast, Figure 10f shows uniform black dots on the surface of the LBO-coated LNMO particles, attributed to the low-atomic-mass borate coating. Full cells employing pristine or LBO-coated LNMO as cathodes and commercial graphite as the anode demonstrated striking differences in cycling performance. After 1000 cycles at 0.3 C, the capacity retention of the uncoated LNMO was only 18.1%, compared to 46.1% for the LBO-coated counterpart (Figure 10g). Moreover, the LBO-coated LNMO exhibited a more stable charge–discharge voltage profile throughout cycling (Figure 10h), confirming its enhanced electrochemical stability. Collectively, these studies offer valuable insights into the stabilization of spinel cathodes through surface coatings, highlighting the potential of single-crystal LNMO for practical battery applications.

2.7. Cobalt-Free Li- and Mn-Rich Layered Type Single Crystal Cathodes

Layered oxide $Li[Li_{1/3}Mn_{2/3}]O_2$, commonly written as Li_2MnO_3 (LMO), adopted an AB_2O_3-type monoclinic structure with C2/m space group and offered a theoretical capacity of up to 458 mA h g^{-1}.[138–142] Structurally, LMO resembled the O3-type layered structure typical of $LiCoO_2$, where "O" referred to octahedral coordination of the cations and "3" denoted the presence of three MO_2 slabs per unit cell. In this structure, the TM layers contained Li^+/Mn^{4+} in a 1:2 molar ratio, separated by cubic-close-packed oxygen planes.[143,144] The conventional formula for this O3-type layered structure can be represented as $Li_{3a}[Li_{1/3}Mn_{2/3}]_{3b}O_2$, where the lithium ions occupied the interslab octahedral sites while the Li^+ and Mn^{4+} ions (in the ratio 1:2) and 3*a* and 3*b* octahedral sites of the trigonal lattice.[145] Due to the large charge difference between Li^+ and Mn^{4+} ions, LMO exhibited superstructure reflections arising from their cation ordering within the TM layers.[146,147] However, depending on the sintering temperature, LMO can crystallize in two distinct phases: the α-phase, in which Li^+ and Mn^{4+} were randomly distributed across the cation sites, and the β--phase, characterized by perfect cation ordering.[145] Despite its promising theoretical capacity, a major limitation of LMO was its electrochemically inactivity within the typical voltage range 2.2–4.4 V *vs.* Li^+/Li as all Mn atoms existed in +4 valence, making further oxidation difficult in an octahedral coordination environment.[148–150] As a result, lithium could not be readily extracted under typical cycling conditions. To activate the material, an initial charge to a high cut-off voltage (~4.8 V vs. Li^+/Li) was required, which triggered the removal of lithium oxide (Li_2O) via the following reaction:

$$Li_2MnO_3 \rightarrow xLi_2O + (1-x)MnO_2 \quad (2)$$

The release of lattice oxygen due to anionic redox reactions could trigger several adverse effects, including structural degradation and TM dissolution, issues that were especially pronounced in polycrystalline LMLOs. Moreover, the primary particles in polycrystalline LMLOs undergo anisotropic volume changes during electrochemical cycling. These variations can lead to severe internal strain accumulation and the development of microcracks, which progressively degrading the solid–solid contact within and between primary particles. This mechanical instability, in turn, amplified interface side reactions and contributed to performance decay over prolonged cycling. In contrast, single-crystal particles, which have a well-ordered structure, are commonly used in Ni-based cathode materials and were known to resist damage during battery cycling. First, their low surface area helps reduce unwanted chemical reactions on the surface, which protects the structure over time. Second, because they have fewer grain boundaries and stronger mechanical stability, they can better handle the stress and strain caused by volume changes during charging and discharging. This makes single-crystal materials more thermally and structurally stable, especially in LMLOs. However, there are handful of reports on lithium-rich manganese-based single crystal cathodes, especially Co-free. For instance, Liu et al. synthesized micron-sized molten-salt-assisted single-crystal Li-rich Mn-based cathode material ($Li_{1.2}Mn_{0.533}Ni_{0.267}O_2$) via a

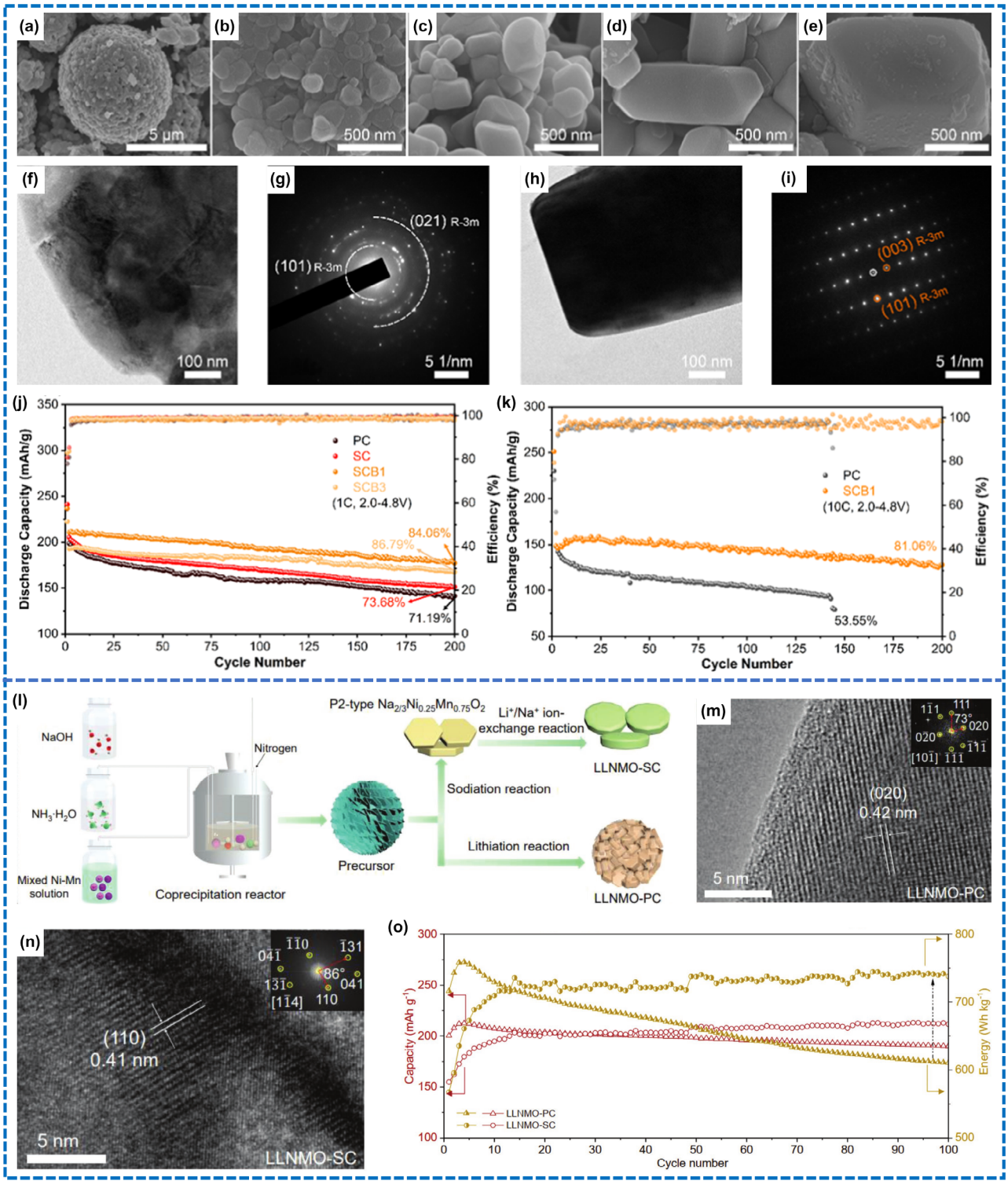

Figure 11. a, b) SEM images of the polycrystalline powder. c–e) SEM images of single-crystalline powder. f) TEM image and g) SAED pattern of the polycrystalline powder. h) TEM image and i) SAED pattern of the single-crystalline powder. j, k) Cycling performance comparison of polycrystalline and single-crystalline sample at 1.0 and 10.0 C, respectively, in a voltage window of 2.0–4.8 V. a–k) were reproduced with permission.[151] Copyright 2024, American Chemical Society. l) Detailed synthesis mechanism of polycrystalline and single-crystalline $Li_{1.2}Mn_{0.6}Ni_{0.2}O_2$ cathode. m, n) HRTEM image and corresponding Fast Fourier Transform (FFT) of polycrystalline and single-crystalline samples, respectively. o) Comparison of specific discharge capacity and energy density retention for polycrystalline and single-crystalline electrodes cycled between 2.0 and 4.8 V at 25 °C.[152] l-o) were reproduced with permission. Copyright 2023, Advanced Science.

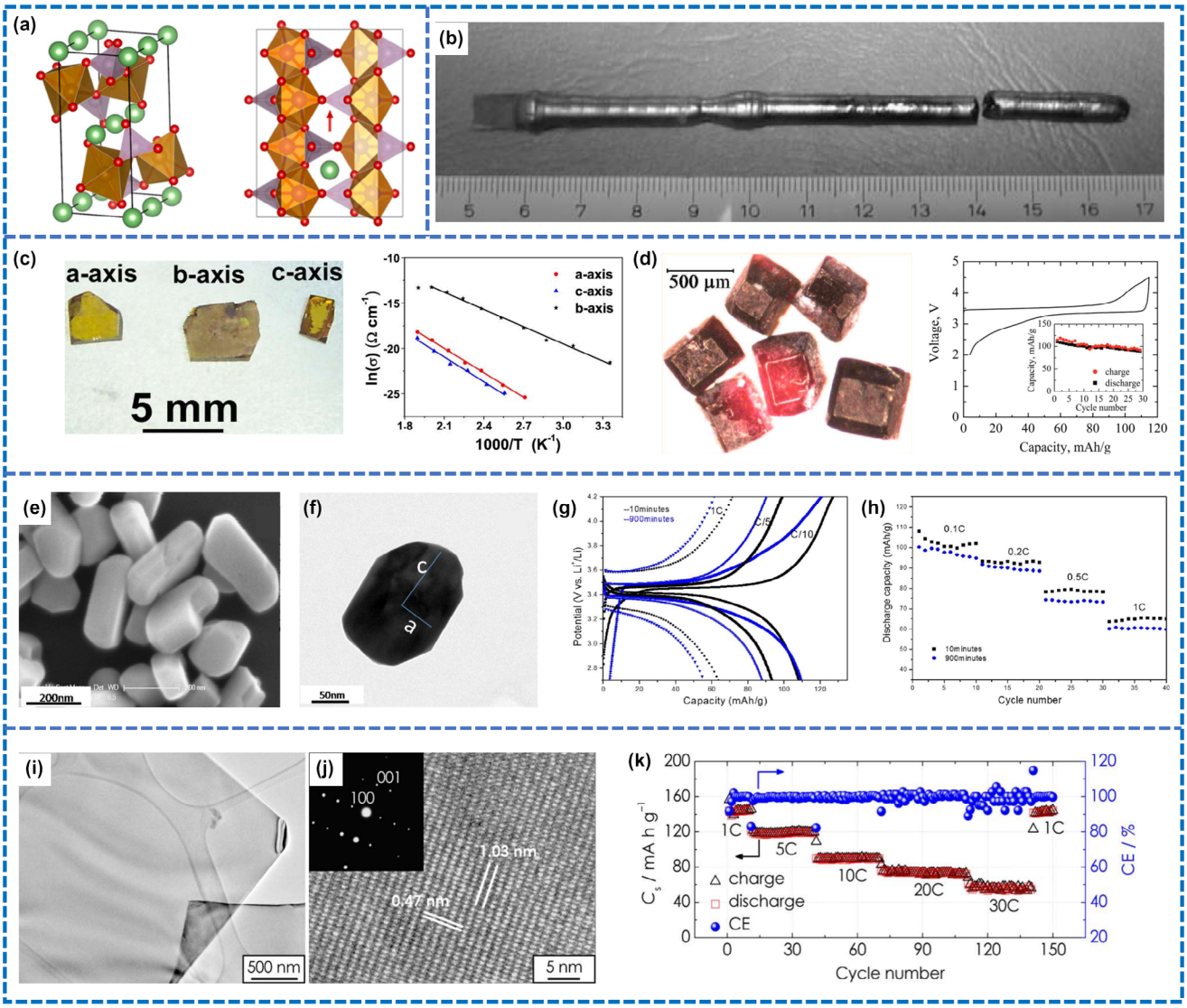

Figure 12. a) Crystal structure of the olivine-type cathode with MO_6, and PO_4 polyhedral are represented in brown and purple color, respectively, while oxygen atom are shown in green color (left panel) and 1-dimensional pathway for Li-ion diffusion in Olivine structure (right Panel).[168] Copyright 2017, MDPI. b) Digital image of the as-grown $LiFePO_4$ single crystal ingot.[185] Copyright 2005, Elsevier. c) Digital photographs of $LiFePO_4$ single crystals thin plates with *a*, *b* and *c*-axes normal the gold-coated surfaces (left panel) and the temperature dependent lithium conductivities along three principal axes with Arrhenius relation fit.[178] Copyright 2008, Elsevier. d) Digital photograph of large $LiFePO_4$ single crystals with size 400 × 300 × 100 μm (left panel) and galvanic cycling between 2.0–4.5 V at 0.1 mA cm^{-2} (right panel); inset shows capacity retention over first 30 cycles.[186] Copyright 2011, American Chemical Society. e) SEM micrograph of single crystalline $LiFePO_4$ synthesized at 160 °C for 900 min. f) Bright field TEM image. g) galvanostatic charge/discharge profiles of polycrystalline and single crystalline $LiFePO_4$. h) Rate performance at various current rates. e–h) were reproduced with permission.[187] Copyright 2013, American Chemical Society. i) TEM and j) HR-TEM images along with the associated ED pattern of the $LiFePO_4$ nanosheets. k) Rate capability at the C-rate ranging from 1 to 30 C. i–k) were reproduced with permission.[188] Copyright 2014, American Chemical Society.

one-step oxalic acid-based complexation route, employing low-melting-point lithium nitrate ($LiNiO_3$) and trace boric acid (H_3BO_3) as additives to promote crystal growth.[151] The resulting single-crystal nanostructures were compared with polycrystalline counterparts in terms of morphology and electrochemical performance. As shown in the SEM images (**Figure 11**a,b), the polycrystalline sample exhibited spherical secondary particles (~8 μm) composed of ~200 nm primary grains. In contrast, the single-crystal samples displayed well-dispersed polyhedral morphology (Figure 11c–e). These observations were further supported by TEM and SAED analyses for both polycrystalline (Figure 11f,g) and single-crystalline samples (Figure 11h,i). The authors explained that molten salts like $LiNO_3$ and H_3BO_3 formed a transient glassy or molten phase at low temperatures during sintering, enhancing heat and mass transport and promoting primary particle coarsening. Additionally, boron doping results in the formation of stable B–O bonds within the lattice, which suppresses oxygen loss and improves structural stability. As a result, the single-crystal LMLOs achieved a high reversible capacity of 210.8 mA h g^{-1} at 1 C (between

2.0 and 4.8 V), with an impressive initial Coulombic efficiency of 82.82% (Figure 11j). Even at 10 °C, the material retained a discharge capacity of 161.1 mA h g^{-1}, and maintained 81.06% of capacity retention after 200 cycles (Figure 11k). Likewise, Yang et al. reported the synthesis of Co-free single-crystalline Li-rich Mn-based cathode ($Li_{1.2}Mn_{0.6}Ni_{0.2}O_2$) via a Li^+/Na^+ ion-exchange reaction.[152] A comparative polycrystalline sample was prepared by traditional hydroxide co-precipitation and solid-state reaction (Figure 11l). HR-TEM image (Figure 11m) and its corresponding FFT pattern (inset) exhibit an array of points with hexagonal symmetry, indicating a layered structure. In contrast, the HR-TEM (Figure 11n) and the corresponding FFT pattern (inset) confirm the single-crystalline nature. Electrochemical tests showed that the single-crystalline electrode delivered a higher discharge capacity (211 mA h g^{-1}) than the polycrystalline electrode (190 mA h g^{-1}) after 100 cycles. Moreover, the energy density of the single-crystal electrode reached 738 Wh kg^{-1}, outperforming its polycrystalline counterpart (612 Wh kg^{-1}). The authors observed that a single crystalline sample demonstrated lower unit cell volume changes (~1.1%) during cycling, facilitating structural robustness. In single-crystal Co-free Mn-rich layered oxide cathodes, both lattice doping and surface modification act as crucial design routes to improve Li^+ transport and preserve oxygen stability during charge–discharge cycling. The substitution of multivalent cations such as Mg^{2+}, Ti^{4+}, Zr^{4+}, W^{6+}, and Al^{3+} within the transition-metal framework modifies the local coordination field and strengthens the TM-O bonding network, which helps restrain Jahn–Teller distortion and minimize oxygen loss at high delithiation levels.[153,154] Similarly, anionic substitution by F^- or S^{2-} adjusts the electronic coupling between O 2p and TM 3d orbitals, narrowing the bandwidth and suppressing irreversible oxygen redox reactions.[155,156] These structural perturbations promote faster Li^+ migration by decreasing the diffusion barrier while maintaining a stable yet elastic lattice.[154,156] In parallel, surface coatings composed of Li-conductive or phosphate compounds (e.g., Li_3PO_4, Li_2MoO_4, or $LiTiPO_4$) form robust, ion-permeable interphases that impede surface reconstruction, electrolyte degradation, and transition-metal dissolution.[157–159] The combined influence of internal lattice regulation and external surface stabilization ultimately enhances Li^+ kinetics, mitigates parasitic oxygen activity, and ensures long-term structural integrity under high-voltage cycling in single-crystal Co-free Mn-rich cathode systems. In conclusion, the use of single-crystalline Li-rich Mn-based cathodes offers a promising pathway toward high-energy and structurally robust LIBs. However, further refinement in synthesis techniques and deeper understanding of structure–property relationships are still required for their commercial viability.

2.8. Cobalt-Free Olivine Type Single Crystal Cathodes

Since the revolutionary work of Padhi et al. in 1997, the olivine-type crystal structure has attracted significant global attention from the scientific community as a promising cathode material for rechargeable LIBs.[160–162] The olivine structure, named after the natural mineral group "olivine", follows the general formula X_2YO_4, where X atoms partially occupy octahedral sites and Y atoms reside in 1/8 of the tetrahedral positions within a hexagonal close-packed oxygen matrix. Among these, lithium iron phosphate ($LiFePO_4$) and lithium manganese phosphate ($LiMnPO_4$) are the most prominent members of the $LiMPO_4$ (M = Fe, Mn, Co, Ni, etc.) family. They have been extensively investigated due to their high theoretical capacity of 170 mA h g^{-1}, low cost (being Co-free), structural stability, excellent capacity retention, and environmental benignity.[163–165] Notably, olivine-type phosphates typically adopt an orthorhombic crystal lattice with *Pnma* space group. In this configuration, phosphorus atoms in the PO_4^{3-} unit occupy tetrahedral 4*c* sites, while Fe and Li cations are situated in FeO_6 and LiO_6 octahedral units at the 4*c* and 4*a* sites, respectively.[166,167] Besides, each phosphate unit (PO_4) shares edges with two LiO_6 and one MO_6 octahedron, as shown in **Figure 12a**.[168] The strongly bonded phosphorus, oxygen, and TM, that is, P_{tet}-O-M_{oct} linkage tuned the M^{3+}/M^{2+} redox potential, enabling a flat and practical voltage plateau.[169,170] However, the presence of such strong covalent bonds is also responsible for a wide bandgap (3.58–4.0 eV) and extremely low electronic conductivity (10^{-9} to 10^{-11} S cm^{-1} at room temperature).[171–174] Furthermore, the lithium-ion diffusion coefficient is also relatively low (~10^{-17} to 10^{-14} cm^2 s^{-1}).[175,176] In general, there are three possible lithium-ion diffusion pathways—[010], [001], and [101]- in $LiMPO_4$ compounds.[177] However, first-principle calculations predict that lithium ions have a one-dimensional diffusion channel along the *b*-axis, that is, [010], in contrast to layered and spinel-type cathodes that support multidirectional ion transport.[178,179] To address the poor electronic conductivity of $LiFePO_4$, various strategies such as surface coating and element doping have been widely adopted.[180–183] These approaches enhance electrolyte compatibility and reduce charge transfer resistance. However, mitigating the limitations of unidirectional ion diffusion necessitates precise control over particle size and crystallographic orientation. In this context, developing single-crystal olivine materials offers distinct advantages over their polycrystalline counterparts, including well-ordered crystal structures, absence of grain boundaries, and directional lithium-ion transport. The growth of single-crystal olivine phosphates can be traced back to 2002, when Fomin et al. synthesized $LiMPO_4$ single crystals via a conventional solution growth method in lithium chloride (LiCl) flux.[184] The study was conducted to analyze the magnetic properties of the $LiNiPO_4$ single crystals (1–5 mm^3). Later, Chen et al.[185] utilized a floating zone technique to prepare large, high-quality single crystals, as shown in Figure 12b. These early studies focused primarily on synthesis and structural characterization, with limited electrochemical analyses. In 2008, researchers began exploring the ionic conductivity and diffusion characteristics of olivine single crystals that are crucial for battery applications. For instance, Li et al. prepared $LiFePO_4$ single crystals (Figure 12c; left panel) and reported the ionic conductivities and diffusion activation energies along the three principal crystallographic axes (Figure 12c; right panel).[178] The activation energies for Li-ion diffusion along the three principal axes are extracted as 0.636 ± 0.052, 0.54 ± 0.048 and 0.669 ± 0.054 eV, respectively, confirming a faster one-dimensional diffusion mechanism along the *b*-axis. Subsequently, the lithium deintercalation behavior in $LiFePO_4$ single crystals was also explored by Upreti et al.[186] Authors prepared copper-substituted iron phosphate single crystals of a sufficient size using high-temperature, high-pressure hydrothermal conditions (Figure 12d; left panel). The prepared single crystals deliver an initial charge/discharge capacity of 115/110 mA h g^{-1} at a current density of 0.1 mA cm^{-2} in the voltage window of 2.0–4.5 V, as shown in Figure 12d (right panel). However, the report was limited to a few initial cycle assessments, and no thorough comparison was made with polycrystalline

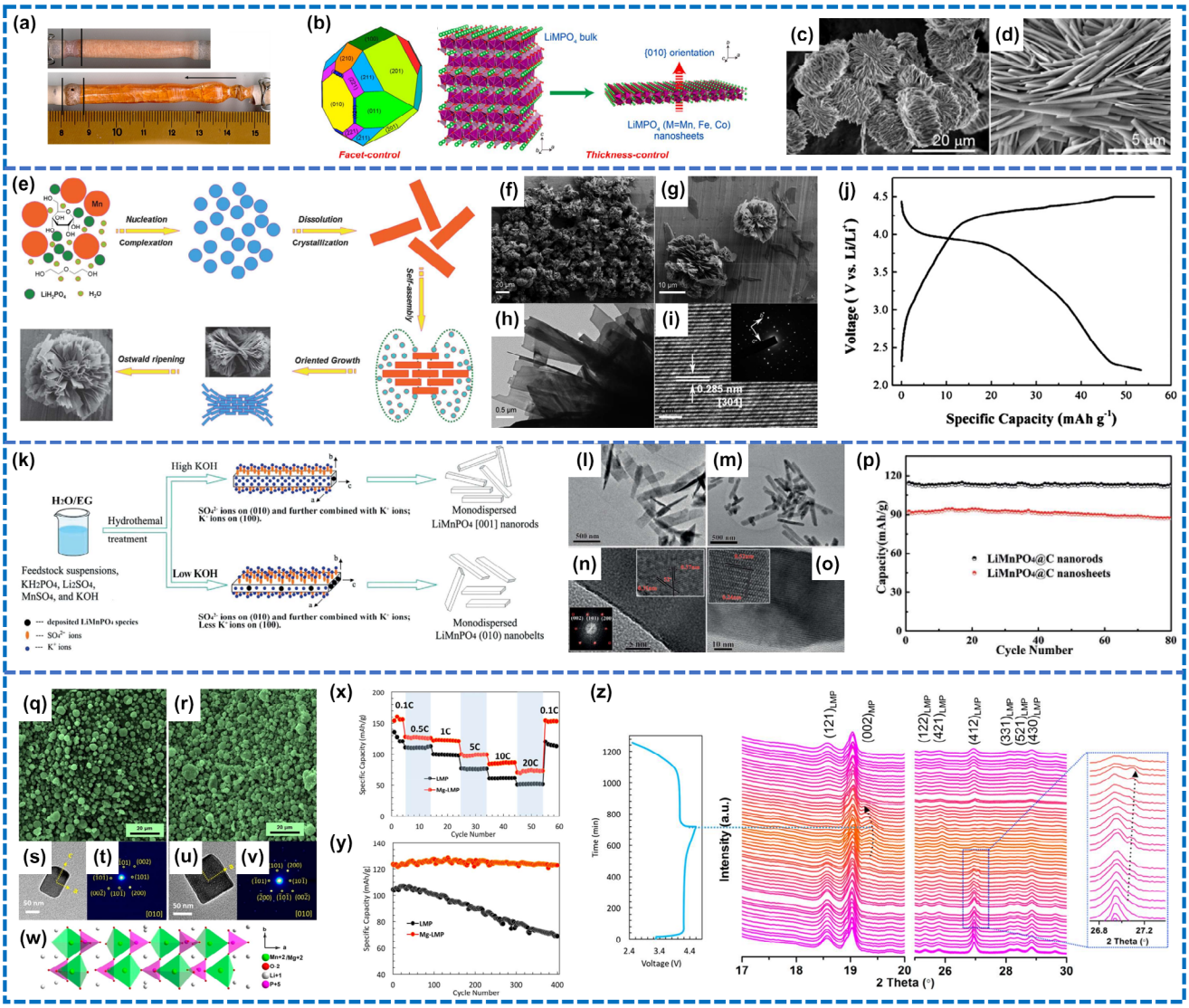

Figure 13. a) Polycrystalline (top) and single crystal $LiMnPO_4$ (bottom) grown using a vertical travelling solvent floating zone (TSFZ).[193] Copyright 2010, Elsevier. b) Wulff structure and schematic illustration of the facet-controlled and thickness-controlled synthesis of single –crystalline $LiMnPO_4$ nanosheets. c, d) SEM images of (010)-oriented $LiMnPO_4$ nanosheets. b–d) were reproduced with permission.[194] Copyright 2017, American Chemical Society. e) Schematic illustration of the growth mechanism of flower-like $LiMnPO_4$ nanostructures. Microstructure of the single crystalline $LiMnPO_4$: f, g) FE-SEM images. h) TEM image. i) HR-TEM image. j) charge/discharge curve at a rate of C/40. e–j) were reproduced with permission.[195] Copyright 2012, Royal Society of Chemistry. k) Schematic illustration of the preparation processes of the monodispersed $LiMnPO_4$ nanobelts and nanorods. l, n) TEM and HR-TEM images of the $LiMnPO_4$ nanobelts. m, o) TEM and HR-TEM images of the $LiMnPO_4$ nanorods. p) cycle performance comparison of the $LiMnPO_4$@C nanobelts and nanorods at 0.1 C. k–p) were reproduced with permission.[196] Copyright 2018, Wiley. q, s, t) SEM and TEM images of $LiMnPO_4$. r, u, v) SEM and TEM images of Mg-doped $LiMnPO_4$. w) Crystal structure of Mg-doped $LiMnPO_4$. x) Comparison of rate performance of the $LiMnPO_4$ and Mg-doped $LiMnPO_4$. y) Long-term cycling performance comparison at 1.0 C. z) Phase transformation of the Mg-doped $LiMnPO_4$ during 1st cycle at 0.1 C. q–z) were reproduced with permission.[197] Copyright 2018, American Chemical Society.

samples. Zhu et al. reported the synthesis and nanostructural evolution of both polycrystalline and single-crystalline $LiFePO_4$ nanostructures using a solvothermal method in a mixed water–tri (ethylene glycol) solvent system.[187] Initially, thin platelets (~100 nm) of $Fe_3(PO_4)_2{\cdot}8H_2O$ (vivianite, VTE) were formed. These metastable VTE surfaces served as nucleation sites for the formation of ~20 nm $LiFePO_4$ nanoparticles. As the reaction progressed and the solution pH gradually decreased, the primary $LiFePO_4$ nanocrystals aggregated via oriented attachment (OA) into polycrystalline, diamond-like secondary particles. Continued pH reduction induced a dissolution–recrystallization process characteristic of Ostwald ripening (OR), ultimately resulting in the formation of monodisperse, single-crystalline $LiFePO_4$ nanorods (450 ± 60 nm long × 128 ± 24 nm wide × 91 ± 13 nm thick), as shown in Figure 12e,f. However, both polycrystalline and single-crystal samples exhibited similar electrochemical performance, as displayed in Figure 12g,h. It is well known that reducing the particle size of $LiFePO_4$ to the nanoscale significantly enhances, its

Table 3. Electrochemical performance comparison of various single crystal olivine-type $LiMPO_4$ (M = Fe, Mn, Ni) cathodes.

Single crystal material	Brief description	Synthesis method	Discharge capacity (mA h g^{-1})/C-rate	Capacity retention (%)/ cycle number	References
$LiFePO_4$	A floating zone technique was used to grow $LiFePO_4$ single crystals sized up to 5 × 70 mm	Floating zone growth	–	–	[185]
Mn substituted $LiFePO_4$	A range of Mn-substituted carbon-coated single crystalline nanotubular and nanoparticular $LiFe_{1-x}Mn_xPO_4$ ($x = 0$, 0.2, and 0.5) cathodes were synthesized and analyzed for Li^+ diffusion and electrochemical properties	Surfactant based sol–gel	45.0/10.0 C	88/1000	[204]
$LiFePO_4$	Surfactant aided sol–gel method is used to fabricate highly crystalline carbon-coated $LiFePO_4$ with bamboo-like single crystalline nanotubes (LFP-NT) obtained using template-assisted method. The prepared nanostructure delivers superior rate capability and excellent cycling stability	Sol–gel	100.0/10.0 C	100/1000	[205]
$LiFePO_4$	A hydrothermal method was adopted to synthesized Cu-substituted $LiFePO_4$ with 15% of the iron sites occupied by cupric ions	Hydrothermal	110/0.1[a]	73/30	[186]
$LiFePO_4$	A low crystal mismatch strategy was embraced to synthesize $LiFePO_4$ nanomesh. The prepared 2D nanomesh demonstrated ultra-high rate capability and extended cycling stability	Hydrothermal	163/0.3[b]	100/3000	[206]
$LiFePO_4$	In situ carbon-coated $LiFePO_4$ nanowires with diameters of around 100 nm produced via electrospinning. These nanowires are single-crystalline and show good electrochemical performance	Electrospinning	170/1.0 C	98/100	[207]
$LiFePO_4$	Single crystalline $LiFePO_4$ nanosheets constituting large proportions of highly oriented (010) facets were prepared via hydrothermal method. The prepared nanosheets display significant capacities even at high C-rates	Hydrothermal	90/10.0 C	100/1000	[188]
$LiFePO_4$	Synthesis and nanostructural development of polycrystalline and single crystalline $LiFePO_4$ nanostructure was carried out using a solvothermal media	Hydrothermal	62/1.0 C	100/10	[187]
$LiFePO_4$	The conductivity of lithium ions along three principal axis directions in single crystal $LiFePO_4$ as a function of temperature by AC impedance spectroscopy is reported	Flux growth technique	–	–	[178]
$LiMnPO_4$	A low temperature solvothermal method was employed to synthesize 3-D hierarchical flower-like $LiMnPO_4$ microspheres. The lithium storage properties reveal its potential application as cathode	Solvothermal	53/0.025 C	–	[195]
$LiMnPO_4$	Single-crystalline (010)-oriented $LiMnPO_4$ nanosheets have been synthesized via solvothermal technique. A systematic investigation of Li ion diffusion using various techniques revealed that facet-controlled nanosheets facilitate diffusion	Solvothermal	120/5.0 C	100/500	[194]
$LiMnPO_4$	Single crystalline rod-like $LiMnPO_4$ nanostructure was prepared via facile solvothermal approach in a mixed solvent of ethylene glycol (EG) and water. The composite nanorods exhibits high specific discharge capacity and a remarkable stable capacity retention	Solvothermal	144/0.5 C	95/100	[208]
$LiMnPO_4$	Highly monodispersed single crystalline $LiMnPO_4$ nanorods were prepared via hydrothermal method. The prepared architecture exhibits excellent discharge capacity and cycling stability	Hydrothermal	114/0.1 C	99/80	[196]
$LiMn_{1-x}Fe_xPO_4$	Fe-substituted $LiMnPO_4$ nanomaterials were synthesized via solvothermal method. The as-prepared $LiMn_{0.8}Fe_{0.2}PO_4$ sample demonstrated excellent cycle performance and remarkable rate capability	Solvothermal	123/0.5 C	100/70	[209]
Fe-doped $LiNiPO_4$	Single crystal hierarchical Fe-doped $LiNiPO_4$ nanomesh is prepared via super-low crystal mismatch at room temperature. The prepared cathode high specific capacity, superior cyclic stability, and excellent rate performance	Solvothermal and Ion Exchange	150/0.1 C	88/100	[210]

[a]mA cm^{-2}.
[b]A g^{-1}.

power density, primarily due to the shortened lithium-ion diffusion pathways within its one-dimensional channels. Nevertheless, downsizing introduces trade-offs: the reduced particle size lowers the tap density and volumetric energy density, while the increased surface area amplifies undesirable side reactions at the electrode–electrolyte interface, compromising cycling stability. In this regard, Zhao et al. prepared single crystalline nanosheets through the exfoliation of bulk $LiFePO_4$ powders.[188] The authors confirmed the single-crystalline nature of the as-exfoliated $LiFePO_4$ nanosheets using TEM, as shown in Figure 12i, which firmly demonstrates that the nanosheet in which the ripple-like contrast revealed their ultrathin nature. Besides, the HR-TEM image and electron diffraction (ED)

pattern (Figure 12j) further validated the single-crystalline nature of the nanosheets. The prepared single-crystal nanosheets, when employed as electrodes, exhibited exceptional rate capability tests, as displayed in Figure 12k. Even at an ultra-high C-rate of 30 °C, the material displayed a considerable discharge capacity of approximately 55 mA h g^{-1}, indicating improved electronic conductivity and reduced diffusion path of lithium ions. In contrast, the commercial $LiFePO_4$/C powders were barely rechargeable at this current rate. The above discussion underscores the performance benefits of single crystals, though scaling up their synthesis remains a challenge.

Likewise, Co-free $LiMnPO_4$-an isostructural analog of $LiFePO_4$- was also explored as a promising cathode material due to its higher energy density than $LiFePO_4$, which primarily comes from its high operating voltage (~4.1 V vs. Li^+/Li) and matches well with most conventional liquid electrolytes.[189,190] However, its practical deployment was limited by intrinsically slow electrochemical kinetics. These kinetic barriers are primarily attributed to 1) surface passivation during delithiation which hinders lithium-ion transport, 2) Jahn–Teller-induced anisotropic lattice distortion arising from high-spin Mn^{3+} ions, 3) lattice strain at phase boundaries between $LiMnPO_4$ and $MnPO_4$ during cycling, and 4) the thermodynamic metastability of the $MnPO_4$ phase.[191,192] Together, these factors contribute to poor rate performance and limited cycling stability. Therefore, it is of great significance to explore new methods and design facile routes to fabricate $LiMnPO_4$ hierarchical architectures with well-defined morphologies. Nevertheless, limited success has been achieved for the general facet-controlled or single crystal synthesis of $LiMnPO_4$. Wizent et al. reported the growth of single crystal $LiMnPO_4$ using the float zone method under high pressure, as shown in **Figure 13**a.[193] However, the work was strictly restricted to the synthesis process only. Likewise, Peng et al. prepared the facet-controlled synthesis of single crystalline $LiMnPO_4$ nanosheets (also including $LiFePO_4$ and $LiCoPO_4$) with a uniform thickness distribution of 15–20 nm using a facile solvothermal process by employing diethyl glycol (DEG) as the solvent, as shown in Figure 13b–d.[194] The authors suggested that the presence of DEG is very crucial for the facet growth as it has a strong bonding with the Mn cation on the (010) facet and inhibits the growth along the (010) direction, where the thickness of the nanosheets was readily controlled by adjusting the Mn and P source ratio. However, the work restricted the electrochemical performance mainly to single crystal $LiFePO_4$ nanosheets. Nie et al. prepared the well-defined three-dimensional hierarchical flower-like $LiMnPO_4$ microspheres via a simple one-step low-temperature solvothermal method, as shown in Figure 13e.[195] Besides, the morphological characterization results in Figure 13f,g firmly validate the formation of flower-like microspheres ($\varphi =$ 10–20 μm), which are primarily composed of crosslink nanoplates with a thickness of several tens of nanometers, as shown in Figure 13h. The HR-TEM and SAED pattern in Figure 13i exhibit clear lattice fringes and a d-spacing of 0.285 nm corresponding to the (301) crystal face, respectively, revealing high crystallinity of the $LiMnPO_4$. Figure 13j reveals the typical charge–discharge profile of the flower-like $LiMnPO_4$/C electrode at a rate of C/40 within a voltage window of 2.3–4.5 V. As observed, the flower-like $LiMnPO_4$/C single crystal electrode exhibits low initial charge/discharge capacities of approximately 56/53 mA h g^{-1} with a reversible voltage plateau at 4.1 V. The authors believe that further improvement in the physical and chemical properties is required to obtain different nanostructures with promising electrochemical performances. In this regard, Bao et al. prepared monodispersed single-crystalline $LiMnPO_4$/C nanobelts and nanorods using the hydrothermal route (Figure 13k).[196] The TEM and HR-TEM images in Figure 13l–o clearly show the formation of monodispersed nanobelts and nanorods with a single crystalline character. However, it was observed during long-term cycling performance at 0.1 C (Figure 13p) that $LiMnPO_4$@C nanorods display higher discharge capacity values after 80 continuous cycles. The authors claim that the high discharge capacity and excellent cycling retention of the monodispersed nanorods is primarily due to the highly ordered lattice structure, size reduction along the (100) channel, and good electronic contact arising from full carbon coating. Although, the prepared single crystal nanorods display improved cycling performance at a low C-rate of 0.1 C, the high rate capability and long-term cycling performance (especially at high C-rates) still need to be explored which in turn depends on the nanostructure design strategy. Wang et al. utilized a facile solvothermal method in combination with spray drying and pyrolysis to obtain magnesium-substituted high-orientation $LiMnPO_4$ single crystals.[197] The authors analyze the micro-, nano-, and electronic structures of the Mg-doped sample along with the uniformity of the Mg^{2+} ion substitution at the secondary particle level using transmission X-ray microscopy combined with X-ray absorption near-edge structure. The morphological features reveal that the secondary particles of doped and undoped samples are spherical in shape (average size ~6.0 μm), as shown in Figure 13q,r, respectively, and consist of primary plates with a size of 80 nm (Figure 13s,u). The plates' growth was controlled along the (010) using oleic acid. The structural merits along with the doping result in improved electrochemical performance (Figure 13x,y) with high-rate capability performance (up to 20.0 C) and prolonged cycling stability (to 400 cycles with 100% retention at 1.0 C-rate). The observed improvement in the performance was attributed to the successful substitution of Mg^{2+} in the Mn^{2+} site, as depicted from the in operando XRD results (Figure 13z). **Table 3** summarizes the synthesis method and electrochemical performance of Co-less olivine-type single crystals published previously. There are various reports on $LiNiPO_4$ single crystals also, but they are restricted to the analysis of the magnetic properties only, primarily due to the sluggish kinetics of the electronic and lithium-ion transport for $LiNiPO_4$ cathodes. However, it is noteworthy to mention that $LiNiPO_4$ possesses the highest operating voltage of 5.1 V *vs.* Li/Li^+, the highest energy density as well as the smallest volume change.

3. Challenges and Perspectives

Despite the significant progress in developing cobalt-free single-crystal cathode materials, several critical challenges persist that limit their full-scale implementation in commercial LIBs. In Ni-rich systems, controlling surface reconstruction, oxygen release at high states of charge, and maintaining lithium transport pathways within large crystal domains remain unresolved issues. Mn-rich cathodes, although structurally stable and thermally safe, suffer from voltage fading, TM dissolution, and poor electronic conductivity. $LiFePO_4$-based single crystals offer excellent cycle life and safety, but their limited energy density and rate performance continue to restrict their broader application. Moreover, synthesizing phase-pure, defect-free single crystals with uniform particle size and orientation demands precise control over synthesis parameters, which often complicates scalability and cost-effectiveness. A key challenge across these systems lies in reconciling crystallographic integrity with Li^+ transport efficiency. While the absence of grain boundaries in single crystals enhances mechanical durability and mitigates

intergranular cracking, the resulting large particle size often increases Li^+ diffusion length and limits rate capability, particularly in Co-free Ni-rich and Mn-rich layered oxides where Li^+ diffusion is anisotropic along the (003) direction. Reducing particle size or exposing high-index facets such as (104) and (101) can significantly shorten diffusion pathways and improve ionic accessibility, yet these modifications simultaneously raise surface energy, increase electrolyte reactivity, and accelerate parasitic interfacial reactions. In contrast, olivine-type $LiFePO_4$ demonstrates inherently one-dimensional Li^+ diffusion along the (010) direction, making facet orientation and particle aspect ratio decisive factors in balancing ion mobility and mechanical stability. Spinel-type cathodes ($LiMn_2O_4$ and $LiNi_{0.5}Mn_{1.5}O_4$), on the other hand, benefit from a three-dimensional Li^+ transport framework, but the reduction of surface area in highly crystalline particles can impede electrolyte penetration and reduce interfacial kinetics.

Looking forward, a few strategic directions could accelerate the transition of these materials toward real-world applications. Combining bulk and surface-level modifications such as multi-element doping, facet-selective coatings, and grain boundary regulation will be essential to enhance structural integrity and electrochemical stability under high-voltage and high-rate conditions. In parallel, new synthesis techniques capable of tuning crystallographic orientation and particle morphology at scale are needed. The integration of these materials into next-generation architectures, including solid-state configurations and high-voltage electrolytes, requires a deeper understanding of interfacial dynamics. Addressing these challenges through a combination of experimental insights, computational modelling, and in situ diagnostics will be crucial for the practical realization of safe, cobalt-free, and long-lasting LIBs.

Acknowledgements

Srinivasan Alagar and Rakesh Saroha contributed equally to this work. The authors gratefully acknowledge the financial support provided by the National Research Foundation of Korea (NRF) and the Commercialization Promotion Agency for R&D Outcomes (COMPA) under the Ministry of Science and ICT (Grant Nos. RS-2023-00217581 and RS-2023-00304768). This research was supported by Chungcheongbuk-do Province and the Convergence and Open Sharing System (COSS) Development Project (2025).

Conflict of Interest

The authors declare no conflict of interest.

Data Availability Statement

No experimental data are associated with this manuscript.

Keywords

Co-free cathodes, Li and Mn-rich, Ni-rich layered oxide, olivine cathode, single-crystal structure

Received: September 5, 2025
Revised: October 14, 2025
Published online: October 14, 2025

[1] M. Armand, J. M. Tarascon, *Nature* **2008**, *451*, 652.
[2] B. Dunn, H. Kamath, J.-M. Tarascon, *Science* **2011**, *334*, 928.
[3] V. Etacheri, R. Marom, R. Elazari, G. Salitra, D. Aurbach, *Energy Environ. Sci.* **2011**, *4*, 3243.
[4] J. B. Goodenough, Y. Kim, *Chem. Mater.* **2010**, *22*, 587.
[5] N. Nitta, F. Wu, J. T. Lee, G. Yushin, *Mater. Today* **2015**, *18*, 252.
[6] A. Manthiram, *Nat. Commun.* **2020**, *11*, 1550.
[7] G. E. Blomgren, *J. Electrochem. Soc.* **2016**, *164*, A5019.
[8] M. Li, J. Lu, Z. Chen, K. Amine, *Adv. Mater.* **2018**, *30*, 1800561.
[9] B. Xu, D. Qian, Z. Wang, Y. S. Meng, *Mater. Sci. Eng. R. Rep.* **2012**, *73*, 51.
[10] C. Li, B. Liu, N. Jiang, Y. Ding, *Nano Res. Energy* **2022**, *1*, e9120031.
[11] K. Mizushima, P. C. Jones, P. J. Wiseman, J. B. Goodenough, *Mater. Res. Bull.* **1980**, *15*, 783.
[12] W. Li, B. Song, A. Manthiram, *Chem. Soc. Rev.* **2017**, *46*, 3006.
[13] H. Zhao, W. Y. A. Lam, L. Sheng, L. Wang, P. Bai, Y. Yang, D. Ren, H. Xu, X. He, *Adv. Energy Mater.* **2022**, *12*, 2103894.
[14] N. Voronina, Y.-K. Sun, S.-T. Myung, *ACS Energy Lett.* **2020**, *5*, 1814.
[15] G. L. Xu, X. Liu, A. Daali, R. Amine, Z. Chen, K. Amine, *Adv. Funct. Mater.* **2020**, *30*, 2004748.
[16] J. Ma, P. Hu, G. Cui, L. Chen, *Chem. Mater.* **2016**, *28*, 3578.
[17] W. He, W. Guo, H. Wu, L. Lin, Q. Liu, X. Han, Q. Xie, P. Liu, H. Zheng, L. Wang, *Adv. Mater.* **2021**, *33*, 2005937.
[18] G. Qian, Y. Zhang, L. Li, R. Zhang, J. Xu, Z. Cheng, S. Xie, H. Wang, Q. Rao, Y. He, *Energy Storage Mater* **2020**, *27*, 140.
[19] S.-j. Lu, L.-b. Tang, H.-x. Wei, Y.-d. Huang, C. Yan, Z.-j. He, Y.-j. Li, J. Mao, K. Dai, J.-c. Zheng, *Electrochem. Energy Rev.* **2022**, *5*, 15.
[20] A. Ran, S. Chen, M. Cheng, Z. Liang, B. Li, G. Zhou, F. Kang, X. Zhang, G. Wei, *J Mater Chem A* **2022**, *10*, 19680.
[21] J. Shen, B. Zhang, W. Huang, X. Li, Z. Xiao, J. Wang, T. Zhou, J. Wen, T. Liu, K. Amine, *Adv. Funct. Mater.* **2023**, *33*, 2300081.
[22] Z. Wu, C. Zhang, F. Yuan, M. Lyu, P. Yang, L. Zhang, M. Zhou, L. Wang, S. Zhang, L. Wang, *Nano Energy* **2024**, *126*, 109620.
[23] H.-H. Ryu, S.-B. Lee, C. S. Yoon, Y.-K. Sun, *ACS Energy Lett.* **2022**, *7*, 3072.
[24] Z. Xiao, X. He, F. Yu, B. Zhang, X. Ou, *Nano Lett.* **2024**, *24*, 11358.
[25] C. Wang, R. Yu, S. Hwang, J. Liang, X. Li, C. Zhao, Y. Sun, J. Wang, N. Holmes, R. Li, *Energy Storage Mater* **2020**, *30*, 98.
[26] J. Hu, H. Wang, B. Xiao, P. Liu, T. Huang, Y. Li, X. Ren, Q. Zhang, J. Liu, X. Ouyang, *Natl. Sci. Rev.* **2023**, *10*, nwad252.
[27] J. Gao, C. Ouyang, J. Wang, W. Yu, J. Wang, S. Xu, X. Lv, *Chem. Commun.* **2025**, *61*, 13780.
[28] J. Lu, X. Min, W. Yan, Y. Tang, Y. Liu, R. Mi, W. Wang, Z. Huang, M. Fang, *J Energy Storage* **2025**, *128*, 117221.
[29] T. Mizokawa, Y. Wakisaka, T. Sudayama, C. Iwai, K. Miyoshi, J. Takeuchi, H. Wadati, D. G. Hawthorn, T. Z. Regier, G. A. Sawatzky, *Phys. Rev. Lett.* **2013**, *111*, 056404.
[30] C. Delmas, I. Saadoune, *Solid State Ionics* **1992**, *53*, 370.
[31] Z. Liu, A. Yu, J. Y. Lee, *J. Power Sources* **1999**, *81*, 416.
[32] L. Ma, M. Nie, J. Xia, J. R. Dahn, *J. Power Sources* **2016**, *327*, 145.
[33] T. Ohzuku, Y. Makimura, *Chem. Lett.* **2001**, *30*, 642.
[34] S.-T. Myung, F. Maglia, K.-J. Park, C. S. Yoon, P. Lamp, S.-J. Kim, Y.-K. Sun, *ACS Energy Lett.* **2017**, *2*, 196.
[35] M.-H. Kim, H.-S. Shin, D. Shin, Y.-K. Sun, *J. Power Sources* **2006**, *159*, 1328.
[36] H.-J. Noh, S. Youn, C. S. Yoon, Y.-K. Sun, *J. Power Sources* **2013**, *233*, 121.
[37] J. S. Weaving, F. Coowar, D. A. Teagle, J. Cullen, V. Dass, P. Bindin, R. Green, W. J. Macklin, *J. Power Sources* **2001**, *97*, 733.
[38] C. H. Chen, J. Liu, M. E. Stoll, G. Henriksen, D. R. Vissers, K. Amine, *J. Power Sources* **2004**, *128*, 278.
[39] Y. Cui, H. Yao, J. Zhang, T. Zhang, Y. Wang, L. Hong, K. Xian, B. Xu, S. Zhang, J. Peng, *Nat. Commun.* **2019**, *10*, 2515.
[40] D.-W. Jun, C. S. Yoon, U.-H. Kim, Y.-K. Sun, *Chem. Mater.* **2017**, *29*, 5048.

[41] J. Liu, Y. Yuan, J. Zheng, L. Wang, J. Ji, Q. Zhang, L. Yang, Z. Bai, J. Lu, *Angew. Chem.* **2023**, *135*, e202302547.
[42] L. Liang, M. Su, Z. Sun, L. Wang, L. Hou, H. Liu, Q. Zhang, C. Yuan, *Sci. Adv.* **2024**, *10*, eado4472.
[43] W. Li, S. Lee, A. Manthiram, *Adv. Mater.* **2020**, *32*, 2002718.
[44] A. Aishova, G. T. Park, C. S. Yoon, Y. K. Sun, *Adv. Energy Mater.* **2020**, *10*, 1903179.
[45] T. Ohzuku, A. Ueda, M. Nagayama, *J. Electrochem. Soc.* **1993**, *140*, 1862.
[46] A. Manthiram, J. C. Knight, S. T. Myung, S. M. Oh, Y. K. Sun, *Adv. Energy Mater.* **2016**, *6*, 1501010.
[47] J. Sun, X. Cao, H. Zhou, *Phys. Rev. Mater.* **2022**, *6*, 070201.
[48] C. Xu, P. J. Reeves, Q. Jacquet, C. P. Grey, *Adv. Energy Mater.* **2021**, *11*, 2003404.
[49] F. Wu, N. Liu, L. Chen, N. Li, J. Dong, Y. Lu, G. Tan, M. Xu, D. Cao, Y. Liu, *J. Energy Chem.* **2021**, *62*, 351.
[50] W. Liu, P. Oh, X. Liu, M. J. Lee, W. Cho, S. Chae, Y. Kim, J. Cho, *Angew. Chem. Int. Ed.* **2015**, *54*, 4440.
[51] M. Hong, V.-C. Ho, J. Mun, *Front. Batter. Electrochem.* **2024**, *3*, 1338069.
[52] A. Medvedeva, E. Makhonina, L. Pechen, Y. Politov, A. Rumyantsev, Y. Koshtyal, A. Goloveshkin, K. Maslakov, I. Eremenko, *Materials* **2022**, *15*, 8225.
[53] M. G. Rigamonti, *Spray Drying LiFePO4 Nanoparticle Suspensions and Scale-Up*, Ecole Polytechnique, Montreal, QC **2019**.
[54] K. Du, H. Xie, G. Hu, Z. Peng, Y. Cao, F. Yu, *ACS Appl. Mater. Interfaces* **2016**, *8*, 17713.
[55] S.-B. Kim, S.-Y. Ahn, J.-H. Kim, J.-S. Jang, K.-W. Park, *Electrochem. Commun.* **2023**, *146*, 107426.
[56] H. Ding, X. Wang, J. Wang, H. Zhang, G. Liu, W. Yu, X. Dong, J. Wang, *J. Power Sources* **2023**, *553*, 232307.
[57] L. Wen, F. Cheng, X. Wang, X. Zeng, T. Wang, L. Li, Y. Hu, Q. Yu, W. Lu, *Energy Mater.* **2024**, *4*, 400054.
[58] T. Entwistle, E. Sanchez-Perez, G. J. Murray, N. Anthonisamy, S. A. Cussen, *Energy Rep.* **2022**, *8*, 67.
[59] W. Li, E. M. Erickson, A. Manthiram, *Nat. Energy* **2020**, *5*, 26.
[60] J. Wang, B. Batara, K. Xu, K. Zhang, W. Hua, Y. Peng, W. Liu, A. H. I. Putri, Y. Xu, X. Sun, *Energy Environ. Mater.* **2025**, *8*, e70078.
[61] W. Liang, F. Jin, Y. Zhao, L. Shi, Q. Liu, Z. Wang, Y. Wang, M. Zhang, J. Zhu, S. Yuan, *Chem. Eng. J.* **2023**, *464*, 142656.
[62] J. Li, Z. Zhou, Z. Luo, Z. He, J. Zheng, Y. Li, J. Mao, K. Dai, *Sustain. Mater. Technol.* **2021**, *29*, e00305.
[63] H. Kaneda, Y. Furuichi, A. Ikezawa, H. Arai, *ACS Appl. Mater. Interfaces* **2022**, *14*, 52766.
[64] X. Zhang, Y. Zhang, J. Liu, Z. Yan, J. Chen, *J. Energy Chem.* **2021**, *63*, 217.
[65] L. Ni, R. Guo, S. Fang, J. Chen, J. Gao, Y. Mei, S. Zhang, W. Deng, G. Zou, H. Hou, *eScience* **2022**, *2*, 116.
[66] M. Jiang, D. L. Danilov, R. A. Eichel, P. H. L. Notten, *Adv. Energy Mater.* **2021**, *11*, 2103005.
[67] W. Liu, D. Li, Y. Liu, D. Luo, R. Xu, *Renewables* **2024**, *2*, 25.
[68] H. Zhang, J. Dong, Y. Lu, Y. Liu, J. Hao, N. Li, G. Chen, Q. Huang, Y. Su, F. Wu, *Nano Energy* **2025**, *142*, 111177.
[69] K. Homlamai, N. Anansuksawat, N. Joraleechanchai, P. Chiochan, T. Sangsanit, W. Tejangkura, T. Maihom, J. Limtrakul, M. Sawangphruk, *Chem. Commun.* **2022**, *58*, 11382.
[70] T. Liu, K. Fan, C. Chen, M. Dong, Y. Zhu, G. Chen, J. Li, Z. Lin, L. Li, Y. Zhu, *J Mater Chem A* **2024**, *12*, 12702.
[71] Y. Xia, L. Zhou, K. Wang, C. Lu, Z. Xiao, Q. Mao, X. Lu, J. Zhang, H. Huang, Y. Gan, *J. Solid State Electrochem.* **2023**, *27*, 1363.
[72] S. Aryal, J. L. Durham, A. L. Lipson, K. Z. Pupek, O. Kahvecioglu, *Electrochim. Acta* **2021**, *391*, 138929.
[73] L. Yu, A. Dai, T. Zhou, W. Huang, J. Wang, T. Li, X. He, L. Ma, X. Xiao, M. Ge, *Nat. Commun.* **2025**, *16*, 434.
[74] P. Dai, X. Kong, H. Yang, J. Li, J. Zeng, J. Zhao, *ACS Sustain. Chem. Eng.* **2022**, *10*, 4381.
[75] A. Liu, N. Zhang, J. E. Stark, P. Arab, H. Li, J. R. Dahn, *J. Electrochem. Soc.* **2021**, *168*, 040531.
[76] L. Nie, Z. Wang, X. Zhao, S. Chen, Y. He, H. Zhao, T. Gao, Y. Zhang, L. Dong, F. Kim, *Nano Lett.* **2021**, *21*, 8370.
[77] A. Liu, N. Zhang, J. E. Stark, P. Arab, H. Li, J. R. Dahn, *J. Electrochem. Soc.* **2021**, *168*, 050506.
[78] A. Mesnier, A. Manthiram, *ACS Appl. Mater. Interfaces* **2023**, *15*, 12895.
[79] A. Saleem, H. Zhu, M. K. Majeed, R. Iqbal, B. Jabar, A. Hussain, M. Z. Ashfaq, M. Ahmad, S. Rauf, J. P. Mwizerwa, *ACS Appl. Mater. Interfaces* **2023**, *15*, 20843.
[80] X. Gao, B. Li, G. Rousse, A. V. Morozov, M. Deschamps, E. Elkaïm, L. Zhang, K. Kummer, A. M. Abakumov, J. M. Tarascon, *Adv. Energy Mater.* **2025**, *15*, 2402793.
[81] C. Liang, F. Kong, R. C. Longo, C. Zhang, Y. Nie, Y. Zheng, K. Cho, *J Mater Chem A* **2017**, *5*, 25303.
[82] Y. Wang, G. Du, D. Han, W. Shi, J. Deng, H. Li, W. Zhao, S. Ding, Q. Su, B. Xu, *J. Energy Chem.* **2024**, *91*, 670.
[83] Z.-J. Wu, D. Wang, Z.-F. Gao, H.-F. Yue, W.-M. Liu, *Dalton Trans.* **2015**, *44*, 18624.
[84] W.-C. Kim, J. Kim, J.-H. Kim, D.-H. Park, Y.-Y. Park, J.-S. Jang, S.-Y. Ahn, K. Min, K.-W. Park, *J Mater Chem A* **2024**, *12*, 1135.
[85] Z. Ahaliabadeh, X. Kong, E. Fedorovskaya, T. Kallio, *J. Power Sources* **2022**, *540*, 231633.
[86] J. Zheng, S. Zhao, W. Guan, S. Liao, T. Zeng, S. Zhang, Z. Yue, S. Fang, N. Zhou, Y. Jiang, *Energy Storage Mater* **2025**, *78*, 104251.
[87] S. Yin, W. Deng, J. Chen, X. Gao, G. Zou, H. Hou, X. Ji, *Nano Energy* **2021**, *83*, 105854.
[88] U.-H. Kim, L.-Y. Kuo, P. Kaghazchi, C. S. Yoon, Y.-K. Sun, *ACS Energy Lett.* **2019**, *4*, 576.
[89] Y. J. Guo, C. H. Zhang, S. Xin, J. L. Shi, W. P. Wang, M. Fan, Y. X. Chang, W. H. He, E. Wang, Y. G. Zou, *Angew. Chem.* **2022**, *134*, e202116865.
[90] A. Gomez-Martin, F. Reissig, L. Frankenstein, M. Heidbüchel, M. Winter, T. Placke, R. Schmuch, *Adv. Energy Mater.* **2022**, *12*, 2103045.
[91] L. Ni, H. Chen, W. Deng, B. Wang, J. Chen, Y. Mei, G. Zou, H. Hou, R. Guo, J. Xie, *Adv. Energy Mater.* **2022**, *12*, 2103757.
[92] H. Kang, M. Choi, M. Kim, D. Park, J.-H. Park, W. Choi, *Surf Interfaces* **2023**, *41*, 103304.
[93] Q. Zhang, Y. Chu, J. Wu, P. Dong, Q. Deng, C. Chen, K. Huang, C. Yang, J. Lu, *Adv. Energy Mater.* **2024**, *14*, 2303764.
[94] Y. Liu, Q. Wang, L. Chen, Z. Xiao, X. Fan, S. Ma, L. Ming, A. Tayal, B. Zhang, F. Wu, *Mater. Today* **2022**, *61*, 40.
[95] C. Zeng, R. Zheng, F. Fan, X. Wang, G. Tian, S. Liu, P. Liu, C. Wang, S. Wang, C. Shu, *Energy Storage Mater* **2024**, *72*, 103788.
[96] X. M. Fan, Y. D. Huang, H. X. Wei, L. B. Tang, Z. J. He, C. Yan, J. Mao, K. H. Dai, J. C. Zheng, *Adv. Funct. Mater.* **2022**, *32*, 2109421.
[97] J. Wang, X. Lei, S. Guo, L. Gu, X. Wang, A. Yu, D. Su, *Renewables* **2023**, *1*, 316.
[98] J. Wang, X. Lei, L. Gu, X. Wang, D. Su, *J. Mater. Res.* **2022**, *37*, 3250.
[99] J. Li, W. Li, S. Wang, K. Jarvis, J. Yang, A. Manthiram, *Chem. Mater.* **2018**, *30*, 3101.
[100] F. Reissig, M. A. Lange, L. Haneke, T. Placke, W. G. Zeier, M. Winter, R. Schmuch, A. Gomez-Martin, *ChemSusChem* **2022**, *15*, e202102220.
[101] Q. Deng, Q. Zhang, Y. Chu, Y. Xu, S. You, K. Huang, C. Yang, J. Lu, *Mater. Today* **2024**, *74*, 22.
[102] X. He, J. Shen, B. Zhang, Z. Xiao, L. Ye, Q. Mao, Q. Zhong, X. Ou, *Adv. Funct. Mater.* **2024**, *34*, 2401300.
[103] K. He, J. Liu, Z. Liu, Y. Yang, J. Su, X. Lv, Y. Wen, *ACS Appl Energy Mater* **2024**, *7*, 6475.
[104] J. Shen, B. Zhang, C. Hao, X. Li, Z. Xiao, X. He, X. Ou, *Green Energy Environ.* **2024**, *9*, 1045.

[105] Q. Liu, Z. Wu, J. Sun, R. Xu, X. Li, X. Yu, Y. Liu, *Electrochim. Acta* **2023**, *437*, 141473.
[106] H. Feng, Y. Xu, Y. Zhou, J. Song, J. Yang, Q. Tan, *J. Alloys Compd.* **2024**, *976*, 173043.
[107] T. Liu, K. Fan, Z. Lin, Z. Liang, C. Chen, G. Li, X. Guo, Y. Zhu, G. Chen, H. Li, *J Mater Chem A* **2023**, *11*, 17810.
[108] D. Xia, S. Hu, N. Ding, M. Wen, Q. Xiao, S. Zhong, *Ionics* **2023**, *29*, 1699.
[109] A. Hou, S. Xu, K. Xu, M. Zhang, D. Zhao, *Ionics* **2021**, *27*, 4241.
[110] H. Feng, Y. Xu, Y. Zhou, J. Song, Q. Tan, *ACS Omega* **2024**, *9*, 6994.
[111] P. Pang, X. Tan, Z. Wang, Z. Cai, J. Nan, Z. Xing, H. Li, *Electrochim. Acta* **2021**, *365*, 137380.
[112] J. Ma, X. Huang, R. Huang, Y. Tang, S. Huang, Y. Wang, B. Huang, J. Yang, Y. Li, M. Qin, *J Mater Chem A* **2025**, *13*, 15858.
[113] M. M. Thackeray, W. I. David, P. G. Bruce, J. B. Goodenough, *Mater. Res. Bull.* **1983**, *18*, 461.
[114] W. Tang, X. J. Wang, Y. Y. Hou, L. L. Li, H. Sun, Y. S. Zhu, Y. Bai, Y. P. Wu, K. Zhu, T. van Ree, *J. Power Sources* **2012**, *198*, 308.
[115] D. Tang, Y. Sun, Z. Yang, L. Ben, L. Gu, X. Huang, *Chem. Mater.* **2014**, *26*, 3535.
[116] V. Verhoeven, I. De Schepper, G. Nachtegaal, A. Kentgens, E. Kelder, J. Schoonman, F. Mulder, *Phys. Rev. Lett.* **2001**, *86*, 4314.
[117] Y. Lin, F. Li, K. Zhao, S. Zou, X. Tan, Z. Shi, J. Fan, L. Ouyang, M. Zhu, J. Liu, *Small Methods* **2025**, *9*, 2402233.
[118] H.-Q. Wang, F.-Y. Lai, Y. Li, X.-H. Zhang, Y.-G. Huang, S.-J. Hu, Q.-Y. Li, *Electrochim. Acta* **2015**, *177*, 290.
[119] H. Xia, Z. Luo, J. Xie, *Prog. Nat. Sci. Mater. Int.* **2012**, *22*, 572.
[120] F. Yu, Y. Wang, C. Guo, H. Liu, W. Bao, J. Li, P. Zhang, F. Wang, *Crystals* **2022**, *12*, 317.
[121] J. Akimoto, Y. Takahashi, Y. Gotoh, S. Mizuta, *J. Cryst. Growth* **2001**, *229*, 405.
[122] J. Akimoto, Y. Gotoh, Y. Takahashi, *Cryst. Growth Des.* **2003**, *3*, 627.
[123] E. Hosono, T. Kudo, I. Honma, H. Matsuda, H. Zhou, *Nano Lett.* **2009**, *9*, 1045.
[124] D. K. Kim, P. Muralidharan, H.-W. Lee, R. Ruffo, Y. Yang, C. K. Chan, H. Peng, R. A. Huggins, Y. Cui, *Nano Lett.* **2008**, *8*, 3948.
[125] M. Zhao, X. Song, F. Wang, W. Dai, X. Lu, *Electrochim. Acta* **2011**, *56*, 5673.
[126] Y. L. Ding, J. Xie, G. Cao, T. Zhu, H. Yu, X. Zhao, *J. Phys. Chem. C* **2011**, *115*, 9821.
[127] Y. L. Ding, J. Xie, G. S. Cao, T. J. Zhu, H. M. Yu, X. B. Zhao, *Adv. Funct. Mater.* **2011**, *21*, 348.
[128] D. Zhan, Q. Zhang, X. Hu, G. Zhu, T. Peng, *Solid State Ionics* **2013**, *239*, 8.
[129] Y. Sun, C. Xu, B. Li, J. Xu, Y. He, H. Du, F. Kang, *Int. J. Electrochem. Sci.* **2014**, *9*, 6387.
[130] H. Lin, J. Hu, H. Rong, Y. Zhang, S. Mai, L. Xing, M. Xu, X. Li, W. Li, *J Mater Chem A* **2014**, *2*, 9272.
[131] P. Li, S. h. Luo, J. Wang, X. Wang, Y. Tian, H. Li, Q. Wang, Y. Zhang, X. Liu, *Int. J. Energy Res.* **2021**, *45*, 21158.
[132] H. Park, Z. Guo, A. Manthiram, *Small* **2024**, *20*, 2303526.
[133] J.-S. Kim, K. Kim, W. Cho, W. H. Shin, R. Kanno, J. W. Choi, *Nano Lett.* **2012**, *12*, 6358.
[134] H. Liu, R. Kloepsch, J. Wang, M. Winter, J. Li, *J. Power Sources* **2015**, *300*, 430.
[135] P. Hou, Z. Lin, F. Li, X. Xu, *Small* **2023**, *19*, 2304482.
[136] G. Sun, Z. Song, Y. Dai, Q. Yu, Q. Kang, Z. Wang, Y. Chen, Y. Shi, S. Qiao, Z. Xiao, *Sci. China Mater.* **2025**, *68*, 1.
[137] N. R. Park, Y. Li, W. Yao, M. Zhang, B. Han, C. Mejia, B. Sayahpour, R. Shimizu, B. Bhamwala, B. Dang, *Adv. Funct. Mater.* **2024**, *34*, 2312091.
[138] R. Saroha, A. Gupta, A. K. Panwar, *J. Alloys Compd.* **2017**, *696*, 580.
[139] R. Saroha, J. S. Cho, J.-H. Ahn, *Electrochim. Acta* **2021**, *366*, 137471.
[140] D. Mori, H. Sakaebe, M. Shikano, H. Kojitani, K. Tatsumi, Y. Inaguma, *J. Power Sources* **2011**, *196*, 6934.
[141] S. Kim, C. Kim, J.-K. Noh, S. Yu, S.-J. Kim, W. Chang, W. C. Choi, K. Y. Chung, B.-W. Cho, *J. Power Sources* **2012**, *220*, 422.
[142] R. Saroha, A. K. Panwar, A. Gaur, Y. Sharma, V. Kumar, P. K. Tyagi, *J. Solid State Electrochem.* **2018**, *22*, 2507.
[143] A. Klein, P. Axmann, C. Yada, M. Wohlfahrt-Mehrens, *J. Power Sources* **2015**, *288*, 302.
[144] L. Torres-Castro, J. Shojan, C. M. Julien, A. Huq, C. Dhital, M. P. Paranthaman, R. S. Katiyar, A. Manivannan, *Mater. Sci. Eng. B* **2015**, *201*, 13.
[145] S. F. Amalraj, L. Burlaka, C. M. Julien, A. Mauger, D. Kovacheva, M. Talianker, B. Markovsky, D. Aurbach, *Electrochim. Acta* **2014**, *123*, 395.
[146] Y. Wu, A. Manthiram, *J. Power Sources* **2008**, *183*, 749.
[147] M. Cheng, K. Zhu, L. Yang, L. Zhu, Y. Li, W. Tang, *J. Alloys Compd.* **2016**, *686*, 496.
[148] D. Kim, J. Gim, J. Lim, S. Park, J. Kim, *Mater. Res. Bull.* **2010**, *45*, 252.
[149] C. Park, S. Kim, I. R. Mangani, J. Lee, S. Boo, J. Kim, *Mater. Res. Bull.* **2007**, *42*, 1374.
[150] Q. Zhang, T. Peng, D. Zhan, X. Hu, *J. Power Sources* **2014**, *250*, 40.
[151] K. Liu, Q. Zhang, Z. Lu, H. Zhu, M. Song, L. Chen, C. Zhang, W. Wei, *ACS Appl. Mater. Interfaces* **2024**, *16*, 14902.
[152] X. Yang, S. Wang, D. Han, K. Wang, A. Tayal, V. Baran, A. Missyul, Q. Fu, J. Song, H. Ehrenberg, *Small* **2022**, *18*, 2201522.
[153] A. Choi, J. Lim, H. J. Kim, S. C. Jung, H. W. Lim, H. Kim, M. S. Kwon, Y. K. Han, S. M. Oh, K. T. Lee, *Adv. Energy Mater.* **2018**, *8*, 1702514.
[154] Q. Jiang, X. Li, Y. Hao, J. Zuo, R. Duan, J. Li, G. Cao, J. Wang, J. Wang, M. Li, *Adv. Funct. Mater.* **2025**, *35*, 2400670.
[155] Y. Wang, H.-T. Gu, J.-H. Song, Z.-H. Feng, X.-B. Zhou, Y.-N. Zhou, K. Wang, J.-Y. Xie, *J. Phys. Chem. C* **2018**, *122*, 27836.
[156] X.-M. Zeng, J. Liu, J.-B. Su, F.-H. Wang, Y.-B. Li, C.-J. Zhan, M. Liu, R.-S. Wu, J.-P. Hu, F. Zheng, *RSC Adv.* **2024**, *14*, 26516.
[157] X. Zhang, X. Xie, R. Yu, J. Zhou, Y. Huang, S. Cao, Y. Wang, K. Tang, C. Wu, X. Wang, *ACS Appl Energy Mater* **2019**, *2*, 3532.
[158] Y. Sun, X. Zhang, J. Cheng, M. Guo, X. Li, C. Wang, L. Sun, J. Yan, *Ionics* **2023**, *29*, 2141.
[159] Y. Lei, Y. Elias, Y. Han, D. Xiao, J. Lu, J. Ni, Y. Zhang, C. Zhang, D. Aurbach, Q. Xiao, *ACS Appl. Mater. Interfaces* **2022**, *14*, 49709.
[160] R. Saroha, A. K. Panwar, Y. Sharma, P. K. Tyagi, S. Ghosh, *Appl. Surf. Sci.* **2017**, *394*, 25.
[161] M. Higuchi, K. Katayama, Y. Azuma, M. Yukawa, M. Suhara, *J. Power Sources* **2003**, *119–121*, 258.
[162] S.-P. Chen, D. Lv, J. Chen, Y.-H. Zhang, F.-N. Shi, *Energy Fuel* **2022**, *36*, 1232.
[163] R. Saroha, A. K. Panwar, Y. Sharma, *Ceram. Int.* **2017**, *43*, 5734.
[164] R. Saroha, A. K. Panwar, *J. Phys. D. Appl. Phys.* **2017**, *50*, 255501.
[165] Z. Li, D. Zhang, F. Yang, *J. Mater. Sci.* **2009**, *44*, 2435.
[166] W.-J. Zhang, *J. Power Sources* **2011**, *196*, 2962.
[167] L.-X. Yuan, Z.-H. Wang, W.-X. Zhang, X.-L. Hu, J.-T. Chen, Y.-H. Huang, J. B. Goodenough, *Energy Environ. Sci.* **2011**, *4*, 269.
[168] M. F. Sgroi, R. Lazzaroni, D. Beljonne, D. Pullini, *Batteries* **2017**, *3*, 11.
[169] M. Minakshi, P. Singh, D. Appadoo, D. E. Martin, *Electrochim. Acta* **2011**, *56*, 4356.
[170] W. Zhang, Y. Hu, X. Tao, H. Huang, Y. Gan, C. Wang, *J. Phys. Chem. Solids* **2010**, *71*, 1196.
[171] R. Masrour, E. Hlil, S. Obbade, C. Rossignol, *Solid State Ionics* **2016**, *289*, 214.
[172] G. Xu, K. Zhong, J.-M. Zhang, Z. Huang, *Solid State Ionics* **2015**, *281*, 1.
[173] G. Cai, R. Guo, L. Liu, Y. Yang, C. Zhang, C. Wu, W. Guo, H. Jiang, *J. Power Sources* **2015**, *288*, 136.
[174] H. Shu, X. Wang, W. Wen, Q. Liang, X. Yang, Q. Wei, B. Hu, L. Liu, X. Liu, Y. Song, *Electrochim. Acta* **2013**, *89*, 479.
[175] J. Li, Q. Qu, L. Zhang, L. Zhang, H. Zheng, *J. Alloys Compd.* **2013**, *579*, 377.
[176] R. Qing, M.-C. Yang, Y. S. Meng, W. Sigmund, *Electrochim. Acta* **2013**, *108*, 827.

[177] Wu, B.; Ren, Y.; Li, N., *Electric Vehicles-The Benefits and Barriers*, Seref Soylu, InTech, Sanghai, **2011**, *3*, 199.
[178] J. Li, W. Yao, S. Martin, D. Vaknin, *Solid State Ionics* **2008**, *179*, 2016.
[179] D. Morgan, A. Van der Ven, G. Ceder, *Electrochem. Solid-State Lett.* **2003**, *7*, A30.
[180] H. Zhang, Z. Zou, S. Zhang, J. Liu, S. Zhong, *Int. J. Electrochem. Sci.* **2020**, *15*, 12041.
[181] T.-F. Yi, X.-Y. Li, H. Liu, J. Shu, Y.-R. Zhu, R.-S. Zhu, *Ionics* **2012**, *18*, 529.
[182] K. Akhmetova, F. Sultanov, A. Mentbayeva, N. Umirov, Z. Bakenov, B. Tatykayev, *J. Power Sources* **2024**, *624*, 235531.
[183] L. Li, L. Wu, F. Wu, S. Song, X. Zhang, C. Fu, D. Yuan, Y. Xiang, *J. Electrochem. Soc.* **2017**, *164*, A2138.
[184] V. Fomin, V. Gnezdilov, V. Kurnosov, A. Peschanskii, A. Yeremenko, H. Schmid, J.-P. Rivera, S. Gentil, *Low Temp. Phys.* **2002**, *28*, 203.
[185] D. Chen, A. Maljuk, C. Lin, *J. Cryst. Growth* **2005**, *284*, 86.
[186] S. Upreti, N. A. Chernova, J. Xiao, J. K. Miller, O. V. Yakubovich, J. Cabana, C. P. Grey, V. L. Chevrier, G. Ceder, J. L. Musfeldt, *Chem. Mater.* **2012**, *24*, 166.
[187] J. Zhu, J. Fiore, D. Li, N. M. Kinsinger, Q. Wang, E. DiMasi, J. Guo, D. Kisailus, *Cryst. Growth Des.* **2013**, *13*, 4659.
[188] Y. Zhao, L. Peng, B. Liu, G. Yu, *Nano Lett.* **2014**, *14*, 2849.
[189] H. Li, X. Xiao, J. Wu, X. Wu, R. Chen, Y. Cao, X. Ai, Z. Chen, *Carbon Neutralization* **2025**, *4*, e70009.
[190] L. Yang, W. Deng, W. Xu, Y. Tian, A. Wang, B. Wang, G. Zou, H. Hou, W. Deng, X. Ji, *J Mater Chem A* **2021**, *9*, 14214.
[191] T. A. Wani, G. Suresh, *J Energy Storage* **2021**, *44*, 103307.
[192] V. Aravindan, J. Gnanaraj, Y.-S. Lee, S. Madhavi, *J Mater Chem A* **2013**, *1*, 3518.
[193] N. Wizent, G. Behr, W. Löser, B. Büchner, R. Klingeler, *J. Cryst. Growth* **2011**, *318*, 995.
[194] L. Peng, X. Zhang, Z. Fang, Y. Zhu, Y. Xie, J. J. Cha, G. Yu, *Chem. Mater.* **2017**, *29*, 10526.
[195] P. Nie, L. Shen, F. Zhang, L. Chen, H. Deng, X. Zhang, *CrystEngComm* **2012**, *14*, 4284.
[196] L. Bao, Y. Chen, G. Xu, T. Yang, Z. Ji, *Eur. J. Inorg. Chem.* **2018**, *2018*, 1533.
[197] L. Wang, H. Zhang, Q. Liu, J. Wang, Y. Ren, X. Zhang, G. Yin, J. Wang, P. Zuo, *ACS Appl Energy Mater* **2018**, *1*, 5928.
[198] M. Kitta, T. Akita, M. Kohyama, *J. Power Sources* **2013**, *232*, 7.
[199] G. Jin, H. Qiao, H. Xie, H. Wang, K. He, P. Liu, J. Chen, Y. Tang, S. Liu, C. Huang, *Electrochim. Acta* **2014**, DOI: 10.1016/j.electacta.2014.10.140.
[200] H. Zhao, F. Li, X. Liu, W. Xiong, B. Chen, H. Shao, D. Que, Z. Zhang, Y. Wu, *Electrochim. Acta* **2015**, *166*, 124.
[201] J. Cao, S. Guo, R. Yan, C. Zhang, J. Guo, P. Zheng, *J. Alloys Compd.* **2018**, DOI: 10.1016/j.jallcom.2018.01.107.
[202] H. Park, A. Manthiram, *J. Phys. Chem. C* **2023**, *127*, 8515.
[203] Z. Qiu, T. Huang, Z. Hu, Z. Zhang, *Ionics* **2023**, *29*, 3907.
[204] A. K. Budumuru, M. Viji, A. Jena, B. Nanda, C. Sudakar, *J. Power Sources* **2018**, *406*, 50.
[205] M. Viji, P. Swain, P. S. Mocherla, C. Sudakar, *RSC Adv.* **2016**, *6*, 39710.
[206] Y. Zhang, H. J. Zhang, Y. Y. Feng, L. Fang, Y. Wang, *Small* **2016**, *12*, 516.
[207] C. Zhu, Y. Yu, L. Gu, K. Weichert, J. Maier, *Angew. Chem.* **2011**, *123*, 6402.
[208] Y. Hong, Z. Tang, S. Wang, W. Quan, Z. Zhang, *J Mater Chem A* **2015**, *3*, 10267.
[209] Y. Hong, Z. Tang, Z. Hong, Z. Zhang, *J. Power Sources* **2014**, *248*, 655.
[210] Y. Feng, H. Zhang, L. Fang, Y. Ouyang, Y. Wang, *J Mater Chem A* **2015**, *3*, 15969.